CHALMERS
UNIVERSITY OF TECHNOLOGY

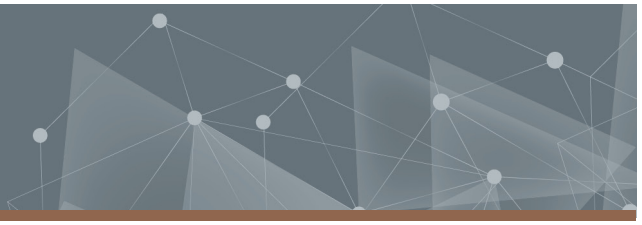

Analysis of Ferrite based PMSM with field strengthening ability

Master's thesis in Electrical Engineering

Karthik Nandi Gopala

DEPARTMENT OF ELECTRICAL ENGINEERING

CHALMERS UNIVERSITY OF TECHNOLOGY
Gothenburg, Sweden 2024
www.chalmers.se

Master's thesis 2024

Analysis of Ferrite based PMSM with field strengthening ability

Karthik Nandi Gopala

CHALMERS
UNIVERSITY OF TECHNOLOGY

Department of Electrical Engineering
Chalmers University of Technology
Gothenburg, Sweden 2024

Analysis of Ferrite based PMSM with field strengthening ability

Supervisor: Torbjörn Thiringer, Department of Electrical Engineering, Chalmers University of Technology
Examiner: Torbjörn Thiringer, Department of Electrical Engineering, Chalmers University of Technology

Master's Thesis 2024
Department of Electrical Engineering
Chalmers University of Technology
SE-412 96 Gothenburg
Telephone +46 31 772 1000

Typeset in LaTeX
Printed by Chalmers Reproservice
Gothenburg, Sweden 2024

Analysis of Ferrite based PMSM with field strengthening ability
Karthik Nandi Gopala
Department of Electrical Engineering
Chalmers University of Technology

Abstract

This thesis focuses on building a FI-PMSM equipped with ferrite magnets. This machine has flux barriers in the rotor design that make the inductance in direct axis greater than the quadrature axis, making the machine to operate primarily in the first quadrant. Further, when the machine enters field weakening operation, the usage of negative d axis current is lower compared to a conventional IPMSM. Theoretically, the working is well suited for a ferrite magnet as there is a lower risk for the magnet to be demagnetised.

Firstly, an FI-PMSM was designed, similar to the one described in a reference paper, to gain a deeper understanding of the machine. As a second step, an IPMSM from a reference paper was selected as a benchmark machine, and the FI-PMSM was scaled to match the dimensions of this motor. After confirming that the machine operated well in its whole operating region, the magnets were replaced with ferrite magnets, and their performance was tested. Subsequently, different rotor designs were explored and tested for performance.

After the theoretical design of the FI-PMSM equipped with ferrite magnets, it was compared with an FI-PMSM equipped with rare-earth magnets, as well as a conventional V-shape IPMSM using ferrite magnets. A comprehensive study was conducted on efficiency, performance, and demagnetization. It was observed that the risk of demagnetization was higher in the FI-PMSM compared to the V-shape IPMSM. Additionally, the V-shape IPMSM equipped with ferrite magnets was found to have similar torque performance to the FI-PMSM equipped with neodymium magnets. However, the FI-PMSM equipped with ferrite magnets demonstrated higher efficiency in the high-speed, low-torque region compared to the V-shape IPMSM.

Keywords: BEV, electric machines, ferrite magnets, field intensifying IPMSM, demagnetisation study.

Acknowledgements

I would like to express my sincere gratitude to Prof. Torbjörn Thiringer for giving me the opportunity to carry out this thesis under his supervision and for placing his trust in me. His guidance, support, valuable feedback, and willingness to share his knowledge have been invaluable throughout this journey. I am also thankful to Emma Grunditz for her support and guidance during the thesis. Lastly, I extend my heartfelt thanks to my family and loved ones for their constant support and encouragement, which helped me complete this work.

Karthik Nandi Gopala, Gothenburg, October 2024

List of Acronyms

Below is the list of acronyms that have been used throughout this thesis:

$i_{\mathrm{d,q}}$	d,q- axis current
$u_{\mathrm{d,q}}$	d,q -axis voltage
$L_{\mathrm{d,q}}$	d,q -axis inductance
$x_{\mathrm{a,b,c}}$	3-phase quantities
x_{α}	quantities in alpha plane
x_{β}	quantities in beta plane
$x_{\mathrm{d,q}}$	quantities in d-q plane
θ_r	transformation angle
R_s	stator resistance
λ_m	magnetic flux linkage
λ_s	stator flux linkage
V_{DC}	battery voltage
I_{max}	maximum current
I_{RMS}	RMS current
T_e	total torque
n_p	number of pole pair
β	current angle
B	flux density
H	applied external field
μ_o	permeability in vacuum
μ_r	relative permeability
H_c	coercive force
ρ	resistivity
N	number of turns in series
l_{total}	total length of winding conductor
A_{cond}	area of conductor
N_{parallel}	number of parallel branches
P_{Cu}	winding losses
P_{I}	iron losses
P_{e}	eddy current losses
P_{h}	hysteresis losses
P_{ee}	excess loss

Contents

1
Background

Electrical machines have been used for a long time in various applications, ranging from small power tools to aerospace propulsion in recent years. Recently, carbon emissions have become a growing concern, with road vehicles being one of the major contributors within the transportation sector. To address this issue, the automotive industry has taken steps toward alternative vehicle propulsion systems, such as electric propulsion, fuel cells, and hydrogen propulsion. However, electric traction motors are commonly used due to their ease of construction, low maintenance, superior performance, and compact packaging.

The IPMSM is a widely adopted motor topology in battery electric vehicles. These motors are efficient, power-dense, and easily controlled. They typically use rare earth metal magnets to produce torque, offering good performance and characteristics. However, these magnets are expensive and have a negative environmental impact when being manufactured[4]. A more affordable and environmentally friendly alternative is ferrite magnets. Although cheaper and greener, ferrite magnets do not match the performance of rare earth magnet machines.

In a conventional IPMSM, the operating region for constant torque is narrow, and in the field weakening region, there is significant use of high negative d-axis current. The use of high negative d-axis current might demagnetize ferrite magnets due to their low coercivity. To ensure smooth operation with ferrite magnets, the FI-PMSM is designed to minimize the use of negative d-axis current. Theoretically, this reduces the risk of irreversible demagnetization and allows the motor to operate smoothly at the same operating points. These machines also have a wider speed range in the constant torque region. The FI-PMSM incorporates flux barriers in the d-direction of the rotor, resulting in a saliency ratio of less than 1.

1.1 Previous work

Previously, several investigations have explored the use of ferrite magnets as an alternative to rare earth metal magnets and the application of FI-PMSM. One such study compared IPMSM and FI-PMSM with rare earth metal magnets[1]. In this investigation, four motors were tested: two IPMSMs and two FI-PMSMs. While the dimensions of these motors were identical, one IPMSM was designed with less magnet mass to match the performance of the FI-PMSM. The IPMSM demonstrated

higher peak torque than the FI-PMSM; however, the FI-PMSM had a broader high torque region and proved to be more efficient at high speeds. The machine operated using less negative d-axis current across the entire operating range, suggesting that it could potentially operate with ferrite magnets. During aggressive driving cycles, the machine showed poor efficiency compared to milder cycles. This study, however, did not include an analysis of FI-PMSM with ferrite magnets or a demagnetization study.

Another investigation was conducted to evaluate the performance of ferrite magnets compared to rare earth magnets in a synchronous reluctance machine[2]. In this research, different rotor geometries were designed and tested to determine whether ferrite magnets could achieve similar performance to rare earth metal magnets. The study found that while the machine was able to match the performance of the machine equipped with rare earth magnet, it required a significantly larger amount of magnet material. This work demonstrates that the use of ferrite magnets as an alternative is feasible, but they are prone to demagnetization due to the use of high negative d-axis currents.

1.2 Purpose of work

This thesis focuses on comparing the performance of an FI-PMSM equipped with ferrite magnet and one equipped with rare earth metal magnets. The FI-PMSM machines are also compared to the performance of a conventional IPMSM. The machine is appropriately scaled to match the performance of the conventional IPMSM, and is slightly redesigned to accommodate ferrite magnets. The goal is to determine the practicality and feasibility of using ferrite magnets instead of rare earth magnets, as the FI-PMSM's characteristics theoretically support the use of ferrite magnets in safe operating conditions.

A demagnetization study is conducted to assess the practicality of using ferrite magnets during short-circuit scenarios. Short circuits can occur due to malfunctions in other components of the electric drive system, which can lead to irreversible demagnetization of the magnets, causing a deterioration in performance of the machine.

2

Theoretical background

The following chapter contains the theoretical background and knowledge for understanding the thesis report.

2.1 Electric Machine

The following section explains the FI-PMSM and characteristics of the machine. It will highlight some similarities and differences between a conventional IPMSM and a FI-PMSM. It gives an overall view of the of design considerations and limitations in designing the machine.

2.1.1 FI-PMSM

Field strengthening or flux intensifying interior permanent magnet synchronous machines were introduced for enhancing the control of flux linkage, for having wider speed range and efficiency over a traditional IPMSM[7]. A notable characteristic of FI-IPMSM machines are the saliency ratio, it is lower than 1, that means that the inductance in the direct axis is greater than the inductance in the quadrature axis throughout the operating region.

These characteristics are facilitated by making design changes to the rotor, by introducing flux barriers in the direction opposite to the quadrature axis of the rotor. The introduction of these flux barriers increases reluctance hence leading to a saliency ratio less than one, i.e, thus making L_d greater than L_q. In this way, it is possible to achieve low flux linkage at higher speeds without the use of high negative I_d currents.

Due to the nature of the machine, maximum torque per ampere is achieved in the first quadrant where I_d is positive. The FI-PMSM from the literature has a rated peak RMS current of 200A and DC link voltage of 364V. The rated torque for this machine is 75 Nm. Figure 2.1 illustrates the operating region of an FI-PMSM that lies in the first quadrant. Figure 2.2 illustrates the torque vs speed and power vs speed curves for the FI-PMSM variant called FS-D, as derived from the literature.

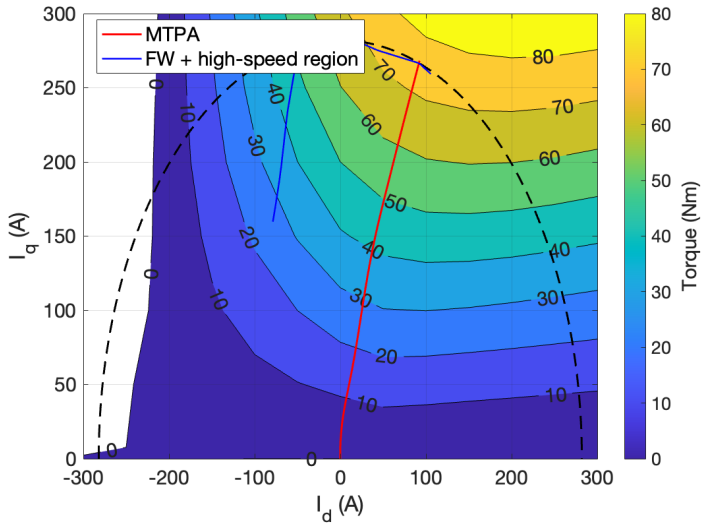

Figure 2.1: Operating region for FI-PMSM from literature

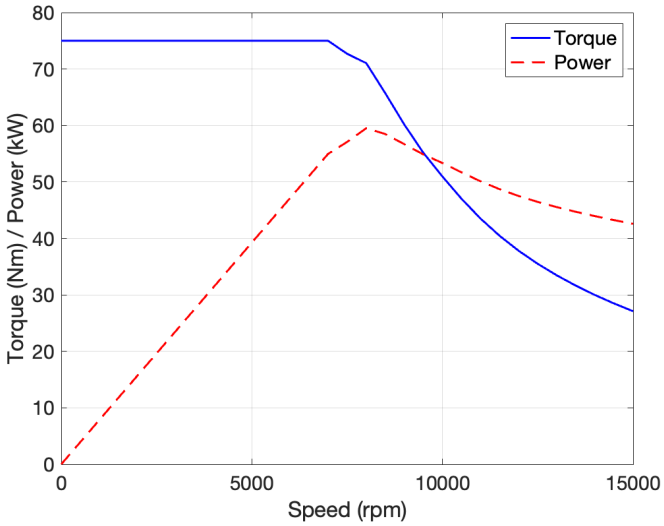

Figure 2.2: Torque vs speed and power vs speed curve for FI-PMSM from literature

During the operation in the first quadrant, the magnetic flux is maintained high even during loaded operation. Unfortunately, the overall torque from the magnetic flux linkage and reluctance torque is seen to be lower than a traditional IPMSM with the same machine dimensions and magnet mass. The requirement for negative I_d is lower in the field weakening region to suppress the flux linkage from the magnets. As a result, efficiency in this region is expected to be higher because less negative I_d is needed to weaken the magnetic flux. This also means that the risk of irreversible demagnetization in the field weakening region is reduced. These characteristics of the machine theoretically support the use of low-coercive magnets.

Figure 2.3 shows the structure of a particular type of FI-PMSM, called FS-D, from [7], among other variants. In this design, the magnet is transversely placed with distributed flux barriers to accommodate leakage flux.

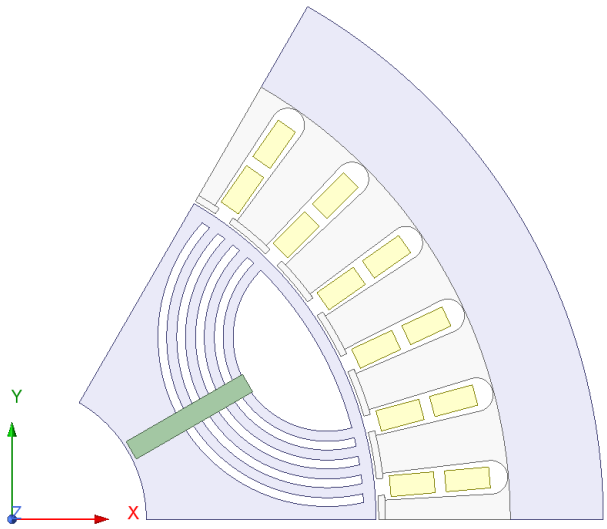

Figure 2.3: Structure of a Field Intensifying Permanent Magnet Synchronous Motor

2.1.2 Equivalent electrical circuit

The machine's physical quantities are initially measured in the three-phase or abc coordinate system, which is later transformed into the $\alpha\beta$ coordinate system using the Clarke transformation

$$\begin{bmatrix} x_\alpha \\ x_\beta \end{bmatrix} = \frac{1}{K} \begin{bmatrix} \frac{2}{3} & -\frac{1}{3} & -\frac{1}{3} \\ 0 & \frac{1}{\sqrt{3}} & -\frac{1}{\sqrt{3}} \end{bmatrix} \begin{bmatrix} x_a \\ x_b \\ x_c \end{bmatrix} \tag{2.1}$$

where x_a, x_b and x_c are quantities in three phase system and the value of K is considered as 1. Further, the quantities can be converted into the dq coordinate system using the Park transformation

$$\begin{bmatrix} x_d \\ x_q \end{bmatrix} = \begin{bmatrix} \cos\theta_r & \sin\theta_r \\ -\sin\theta_r & \cos\theta_r \end{bmatrix} \begin{bmatrix} x_\alpha \\ x_\beta \end{bmatrix} \tag{2.2}$$

where x_α and x_β are quantities in x_α -x_β coordinate system and x_d and x_q d-q coordinate system respectively and θ_r represents the transformation angle. The

electrical machine is analyzed in the dq coordinate system. The dq coordinate system appears stationary with respect to the rotor because its angular velocity matches that of the rotor. The d-axis is aligned with the rotor's magnetic flux linkage, while the q-axis is aligned with the rotor's rotation. This approach makes the signals simplified and easier to study and control the machine. The d axis is responsible for magnetisation and the q axis is responsible for the latent part of the torque production. Figure 2.4 illustrates the process of transformation from rotating vectors to stationary vectors.

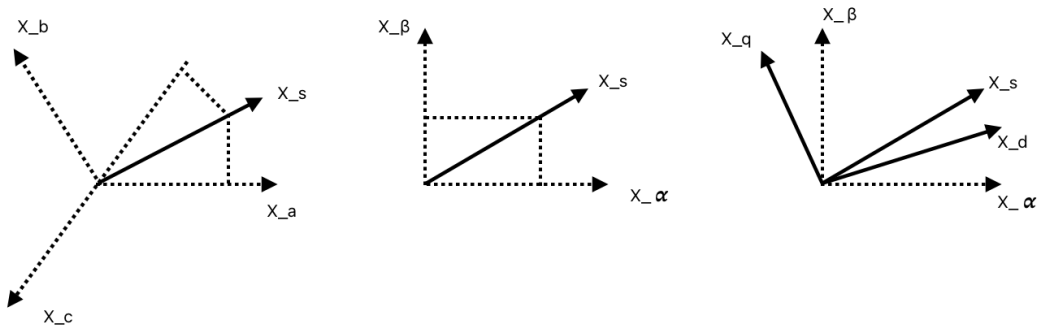

Figure 2.4: Transformation of vectors from rotating to stationary

Figures 2.5 2.6 illustrate the electrical circuits in d-axis and q-axis respectively.

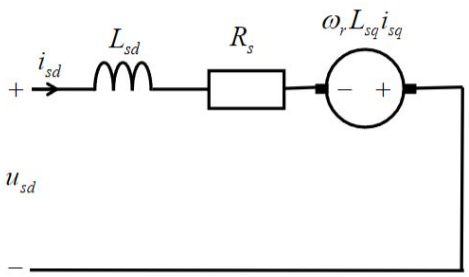

Figure 2.5: Electrical circuit in d axis direction

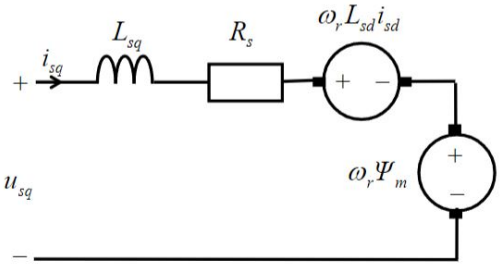

Figure 2.6: Electrical circuit in q axis direction

In figures 2.5 and 2.6, v_{sd} and v_{sq} are the stator voltages in d- and q- axis direction, respectively; i_{sd} and i_{sd} are the currents in d- and q- axis direction, respectively; L_{sd} and L_{sq} are the inductances in d- and q- axis direction, respectively; R_s is the stator winding resistance; ω_r is the electrical speed of the machine and λ_m is the flux due to the magnets. The voltage equations in d- and q- direction are as follows

$$u_{\mathrm{sd}} = R_s i_{\mathrm{sd}} + L_{\mathrm{sd}} \frac{di_{\mathrm{sd}}}{dt} - \omega_r L_{\mathrm{sq}} i_{\mathrm{sq}} \tag{2.3}$$

$$u_{\mathrm{sq}} = R_s i_{\mathrm{sq}} + L_{\mathrm{sq}} \frac{di_{\mathrm{sq}}}{dt} - \omega_r L_{\mathrm{sd}} i_{\mathrm{sd}} + \omega_r \lambda_m \tag{2.4}$$

The electrical speed of the rotor is given by

$$\omega_r = \Omega_r n_{\mathrm{p}} \tag{2.5}$$

where the electrical speed is in radians per second, Ω_r represents the mechanical speed of the rotor, also in radians per second and $n_{\mathrm{p}} is the number of pole pair number$.

2.1.3 Voltage and current limits

The voltage and current is limited by the capacity of the inverter and the current magnitude of the motor respectively

$$\sqrt{v_{\mathrm{sd}}^2 + v_{\mathrm{sq}}^2} \leq \frac{V_{\mathrm{dc}}}{\sqrt{3}} \tag{2.6}$$

$$\sqrt{i_{\mathrm{sd}}^2 + i_{\mathrm{sq}}^2} \leq I_{\mathrm{max}} \tag{2.7}$$

where, v_{sd} and v_{sq} represent the voltages in the d- and q-axis directions, respectively, while V_{dc} denotes the voltage available from the battery. The term $\frac{V_{\mathrm{dc}}}{\sqrt{3}}$ refers to the peak phase voltage. Similarly, i_{sd} and i_{sq} represent the currents in the d- and q-axis directions, respectively, and I_{max} is the maximum current available from the battery.

2.1.4 Torque production

The total torque output of a motor is generated by both the torque produced due to the magnetic flux linkage and the reluctance torque within the motor

$$T_e = \frac{3n_p}{2}(\lambda_m i_{\mathrm{sq}} + (L_{\mathrm{sd}} - L_{\mathrm{sq}}) i_{\mathrm{sd}} i_{\mathrm{sq}}) \tag{2.8}$$

where, λ_m represents the magnetic flux linkage. The first term in (2.8), which is the product of the magnetic flux linkage and i_{sq}, corresponds to the torque produced due to the magnetic flux linkage. The second term, which is the product of the difference between the inductance in the d- and q-axis directions and the stator currents in the d- and q-axis directions, is responsible for the reluctance torque. It can be noted that a higher flux linkage results in higher torque, and a larger difference in inductance also contributes to higher torque. The stator flux linkage equation, which governs the torque production due to magnetic flux linkage, is given by

$$\lambda_s = L_{\mathrm{sd}} i_{\mathrm{sd}} + j L_{\mathrm{sq}} i_{\mathrm{sq}} + \lambda_m \tag{2.9}$$

where λ_s is the stator flux linkage. The inductance in d- and q- axis directions are derived from

$$L_{\mathrm{sd}} = \frac{\lambda_{\mathrm{sd}} - \lambda_m}{i_{\mathrm{sd}}} \tag{2.10}$$

$$L_{\mathrm{sq}} = \frac{\lambda_{\mathrm{sq}}}{i_{\mathrm{sq}}} \tag{2.11}$$

where λ_d and λ_q are the flux linkages in the d- and q- axis directions respectively.

2.2 Permanent Magnets

The following section describes the permanent magnets used, characteristics and its operating region.

Permanent magnets contain several magnetic domains. These domains are initially arranged in a random manner, causing them to cancel each other out, resulting in no net magnetic flux in the absence of external excitation. When an external field is applied to the magnet, the domains align with each other, creating a flux. However, if the external field exceeds the saturation limit, the magnetic domains all align and the flux saturates. Beyond this point, the magnetic domains can no longer return to their original positions causing irreversible demagnetisation. Figure 2.7 illustrates the theory model of magnetic domains within a magnet when partially magnetised, fully magnetised and saturated.

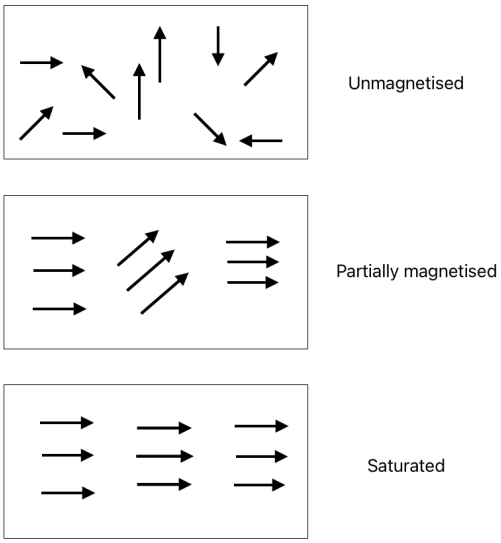

Figure 2.7: Theoretical model of magnetic domain arrangements

The resultant magnetic flux depends on the external field, as

$$B = \mu_0 \mu_r H \tag{2.12}$$

where B is the flux density, μ_0 is the permeability of vacuum, μ_r is the relative permeability, and H is the applied external field. Figure 2.8 represents the characteristics of the resultant flux of a magnet when an external field is applied on it.

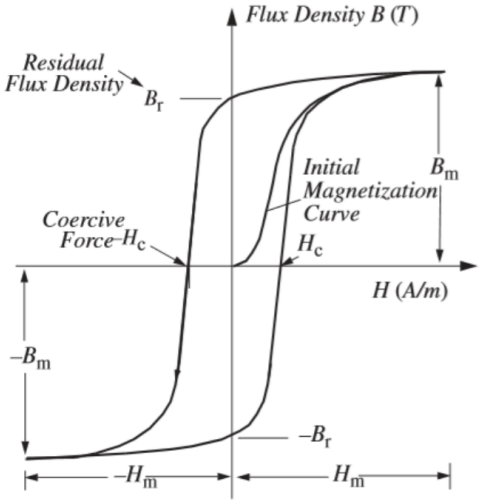

Figure 2.8: Hysteresis loop[2]

When the external field is reversed, the flux starts to drop but lags behind the external field; this phenomenon is known as hysteresis. When the external field reaches zero, the magnet retains some remaining magnetic flux, known as residual or remanent magnetic flux. If a negative external field is applied, the flux continues to decrease until the knee point, after which the magnet undergoes irreversible demagnetization.

2.2.1 Rare earth Magnets

Rare earth magnets are very strong magnets made from alloys. These magnets typically have flux densities greater than 1.2 T, and their saturation points are also very high. They are known for their strong resistance to irreversible demagnetization, meaning that their coercivity (H_c) is higher. These magnets are an attractive material for traction motor applications. However, they are hazardous to the environment and are known to be expensive.

The magnet chosen for this thesis is from the Hitachi's Neomax series. It is a Neodymium-Iron-Boron magnet, known as NMX-37F. Table 2.1 has the necessary

information of the magnet used.

Table 2.1: Rare earth magnet properties

Name	NMX-37F
Manufacturer	Hitachi magnets
Coercive Force(H_c)	-849.2 kA/m
Residual magnetic flux density(B_r)	1.15 T
Relative permeability	1.08
Bulk conductivity	0.67 MSiemens/m

2.2.2 Ferrite magnets

Ferrite magnets are soft magnets that typically have a low flux density, ranging between 0.4 T and 1.02 T. Their coercivity is also very low, meaning that they can be easily demagnetized permanently, which makes their use in traction motors for automotive applications challenging. However, they exhibit excellent magnetic properties at higher temperatures. Ferrite magnets are cheap and environmentally friendly, making them an attractive material for certain applications, however a bit weaker.

The ferrite magnet selected for this thesis is the FB9B magnet from the manufacturer TDK. This magnet was chosen for its high remanent flux and superior performance compared to other ferrite magnets. Table 2.2 describes the properties of the ferrite magnet used.

Table 2.2: Ferrite magnet properties

Name	FB9B
Manufacturer	TDK electronics
Coercive Force(H_c)	-342.2 kA/m
Residual magnetic flux density(B_r)	0.45 T
Relative permeability	1.05
Bulk conductivity	1.5 MSiemens/m

2.3 Field oriented control

Field-oriented control is used to ensure that the machine operates in a safe working condition without damaging other parts of the drivetrain. To achieve the desired torque and minimize losses in the machine, the stator currents in the d- and q-axis directions are controlled using selected strategies in various operating regions. By controlling the d- and q-axis currents, we can regulate both the torque-producing

component and the flux linkage. Two control strategies are implemented to ensure safe operation below and above the base speed. The following section will explain these strategies in detail. Figure 2.9 illustrates different operating regions for a traction motor.

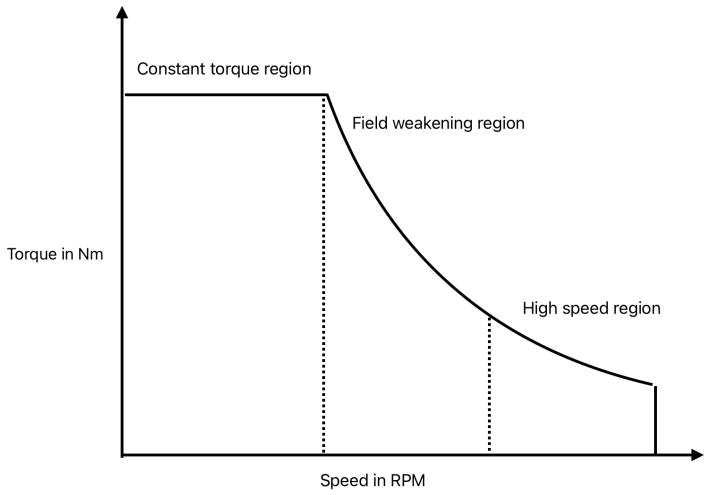

Figure 2.9: Different operating regions of an automotive traction motor

2.3.1 MTPA

The Maximum Torque Per Ampere (MTPA) control strategy is used in the constant torque region before the base speed is reached. This strategy minimizes losses and provides the desired torque output by optimizing the values of i_{sd} and i_{sq}. The relationship between i_{sd} and i_{sq} is

$$i_{\mathrm{sd}} = I \cos \beta \tag{2.13}$$

$$i_{\mathrm{sq}} = I \sin \beta \tag{2.14}$$

where I is the stator current magnitude and β is the current angle. The minimum current magnitude is achieved at a specific current angle, also known as the MTPA current angle. The MTPA angle is the angle between the stator current vector and the d-axis of the rotor.

2.3.2 MTPV

The Maximum Torque Per Voltage (MTPV) control strategy is used in high-speed regions beyond the base speed, where the available voltage is limited due to the increasing back electromotive force (EMF). Since the voltage supply is constrained by the inverter, it can only compensate for the back EMF and induced voltages until the base speed is reached. Afterward, this strategy adjusts the d- and q-axis

current components based on the available maximum voltage. The MTPV strategy is applied until the maximum speed of the motor is reached. Theoretically, the motor speed is infinite, but it is limited by the mechanical components due to friction. Figure 2.10 illustrates the limiting lines MTPA and MTPV control strategies. The circular boundary represents the maximum current magnitude, while the ellipse represents the maximum DC link voltage limit.

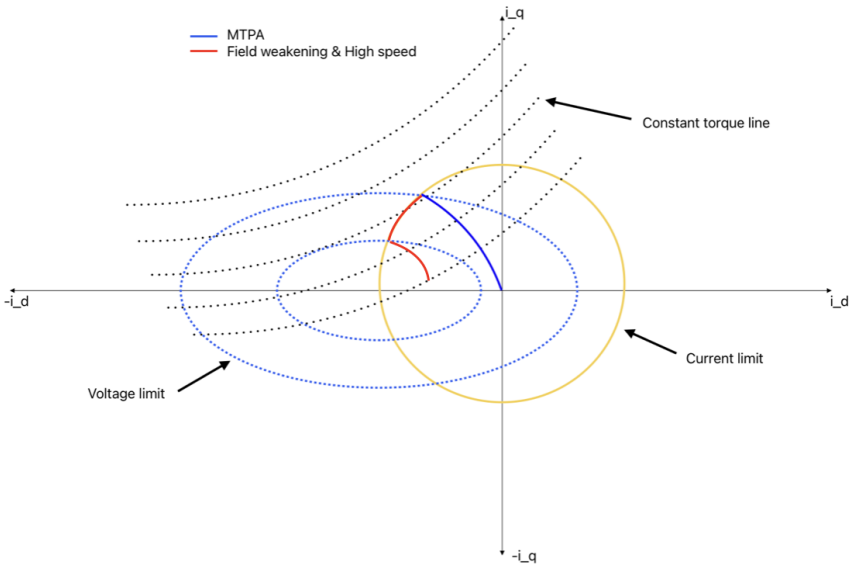

Figure 2.10: Current circle and voltage ellipse

2.4 Field weakening operation

When the motor reaches its rated speed, the constant torque region ends and beyond that point onwards the field weakening region starts. The back electromotive force (EMF) begins to increase as the speed rises, followding the relation

$$e = N\omega_r\lambda_m \tag{2.15}$$

where, e represents the back electromotive force (EMF), N is the number of coil turns in the stator, ω_r is the electrical speed in radians, and λ_m is the magnetic flux linkage. At the rated speed, the stator voltage reaches the maximum value which can be compensated by the DC link voltage. The stator voltage in steady state comprises of different components which is shown below

$$u_{\mathrm{sd}} = R_s i_{\mathrm{sd}} - \omega_r L_{\mathrm{sq}} i_{\mathrm{sq}} \tag{2.16}$$

$$u_{\mathrm{sq}} = R_s i_{\mathrm{sq}} - \omega_r L_{\mathrm{sd}} i_{\mathrm{sd}} + \omega_r \lambda_m \tag{2.17}$$

where the first term makes up for the resistive voltage drop, the second term is the inductive voltage drop and third term is the EMF. In the field weakening region, the d-axis current is adjusted to a negative value to suppress the magnetic flux linkage. This, in turn, reduces torque and enables the motor to increase its rotational speed, a process known as field weakening. In the field weakening region, the power remains constant. However, the negative i_{sd}, also known as the demagnetizing current, is damaging to low-coercive magnets. Excessive negative d-axis current may lead to irreversible demagnetization, exceeding the coercivity limit of the magnets.

2.5 Field strengthening operation

In a conventional IPMSM, the entire operational region lies in the second quadrant, where only negative i_{sd} is used. Since, in a traditional IPMSM, the inductance in the d-axis direction is lower than in the q-axis direction, negative d-axis current is required to produce positive reluctance torque. However, in a FI-PMSM, the inductance in the d-axis direction is greater than in the q-axis direction, meaning positive d-axis current is needed to generate positive reluctance torque, resulting in higher total torque. Therefore, most of the operating region, such as the constant torque region, lies in the first quadrant, where positive i_{sd} is present. To produce a resultant torque, positive d-axis current is used. During machine loading, the magnetic flux is maintained by increasing the positive d-axis current, a phenomenon known as field strengthening operation.. Figure 2.11 illustrates the field strengthening and field weakening operation for a FI- PMSM machine.

2.6 Short circuit & Demagnetization

The IPMSM is the preferred choice of traction motor over other ones for their efficiency. However, there are some disadvantages such as a risk of irreversible demagnetisation of the magnets in the field weakening operation. This is one of the main challenges for IPMSMs equipped with ferrite magnets. There are risks of failures in the driveline that may cause short circuits. Short circuits may be caused by various reasons such as winding insulation failure, inverter components failure, overloading to mention some. Short circuits leads to motor overheating, mechanical damage and failure of the entire drivetrain.

Demagnetization of magnets is what we are most interested in this thesis. When there's a short circuit in the system, a large external field which might be in the wrong direction is sent through the magnet which when is beyond the point of coercivity, the magnet undergoes partial or complete irreversible demagnetisation

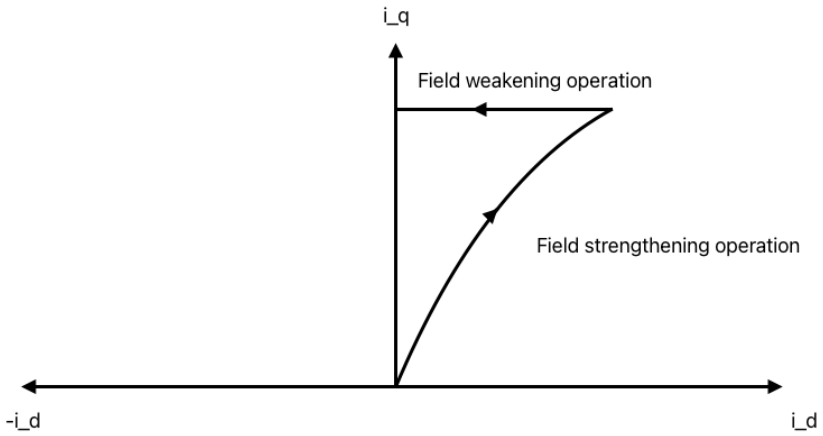

Figure 2.11: Field strengthening operation

leading to failure of the magnets. This leads to increased motor losses, improper control of the motor and it may lead to a complete failure of the motor itself. This is a major concern for ferrite magnets because of the low point of coercivity.

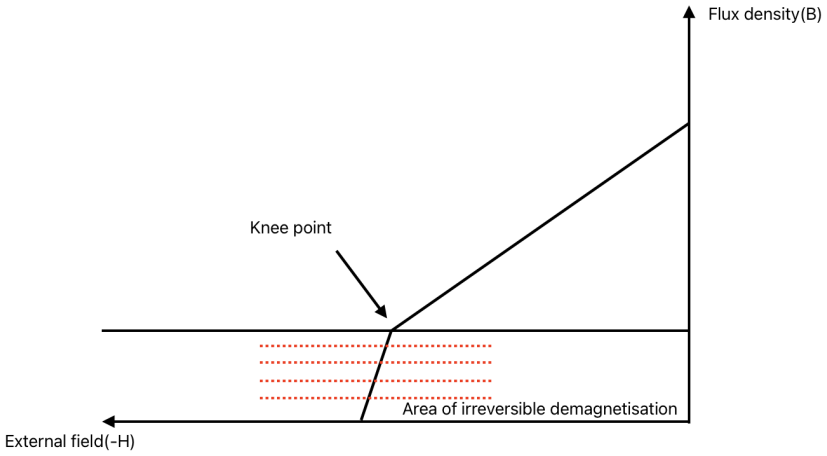

Figure 2.12: Demagnetisation curve

2.7 Losses

IPMSM are known to be efficient and easier to control over induction machines. Since the rotor does not have any windings, there is significant reduction in winding losses in the high torque low speed region. The overall efficiency of the machine is therefore higher. The following section describes the different losses in the machine and how different parameters affect losses.

2.7.1 Winding losses

Winding losses in the stator also known as ohmic losses which are mainly responsible due to the copper coil windings in the stator

$$P_{\text{cu}} = \frac{3}{2K^2} R_s I_{\text{RMS}}^2 \tag{2.18}$$

where R_s is the stator resistance. This is mainly because of the heating in the copper coils. Since the copper windings are present only in the stator, we have lower winding losses in IPMSM. The stator resistance is given by

$$R_s = \rho \frac{l_{\text{total}}}{A_{\text{cond}} N_{\text{parallel}}} \tag{2.19}$$

where ρ is the resistivity of the material, l_{total} is the length of the winding conductor, A_{cond} is the area of the conductor and N_{parallel} is the number of parallel branches.

2.7.2 Iron losses

Based on Bertotti's theory, iron losses consist of eddy losses(Pe), hysteresis loss(P_h) and excess loss(P_{ee}).

$$P_{\text{I}} = P_{\text{e}} + P_{\text{h}} + P_{\text{ee}} \tag{2.20}$$

Eddy losses are considered in stator and rotor. These losses occur due to circulating current in the conducting parts,the fluctuating magnetic flux and the frequency of the current

$$P_{\text{e}} = k_e B_{\text{max}}^2 f^2 \tag{2.21}$$

where k_e is the coefficient of eddy current loss, B_{max} is the peak flux density and f is the frequency. Hysteresis loss is due to the presence of magnetic materials and magnetic fields. This happens due to the lag of magnetic flux as the external field varies.

$$P_{\text{h}} = k_h B_{\text{max}}^2 f \tag{2.22}$$

where, k_h is the coefficient of hysteresis loss factor.

$$P_{\text{ee}} = k_e (B_{\text{max}} f)^{1.5} \tag{2.23}$$

where, k_h is the coefficient of excess loss factor.

3

Case Set-up

This chapter will give the necessary details about geometric dimensions, parameters and other necessary values. This also explains the method of analysis that was used with explanation .

3.1 Initial motor design of FI-PMSM

After the initial literature review, a particular type of FI-PMSM, called FS-D, gained significant interest due to its motor performance and characteristics. In this study, this type of machine exhibited similar performance to a V-shaped IPMSM with the same magnet mass, while demonstrating better efficiency in high-speed, low-torque regions. The machine's rated torque is 75 Nm, which is 14% lower than that of the V-shaped IPMSM, though both machines have almost the same power output of 50 kW. As a result, an initial design of the motor was created and tested to evaluate its performance and operation. Figure 3.1 illustrates the geometry of the FS-D type FI-PMSM referenced in the literature.

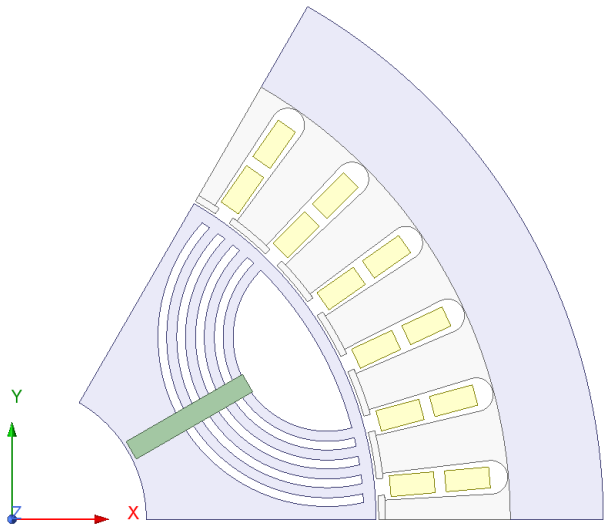

Figure 3.1: Initial geometric design of FI-PMSM

The literature indicates that placing the magnets vertically in this design resulted in 27% higher torque and 18% higher power compared to a design with horizontally placed magnets. The geometric dimensions and other design parameters necessary for constructing the machine are detailed in Table 3.1.

Table 3.1: Design parameters for initial FS-PMSM

Parameter	Value
Stator outer dia(mm)	176.1
Stator inner dia(mm)	109.2
Rotor outer dia(mm)	108.4
Rotor inner dia(mm)	40
Stack length(mm)	100
Number of turns	6
Peak RMS current(A)	200
Max DC link voltage(V)	364
Magnet material	NMX 37 F
Magnet mass(Kg)	0.27

3.2 V shape IPMSM reference motor

As a benchmark machine, a V-shaped IPMSM equipped with Neodymium magnets was used. This motor was referenced in the literature and was inspired by a Prius motor. It has a rated torque of 239 Nm and a power output of 100 kW. To create

suitable benchmark data, the motor was equipped with the same amount of ferrite magnets as the Neodymium magnets used in the literature. The geometric dimensions and other parameters were carried over to rescale the initial FS-PMSM for the starting design. Figure 3.2 illustrates the geomtric design of a V shape IPMSM equipped with neodymium magnets.

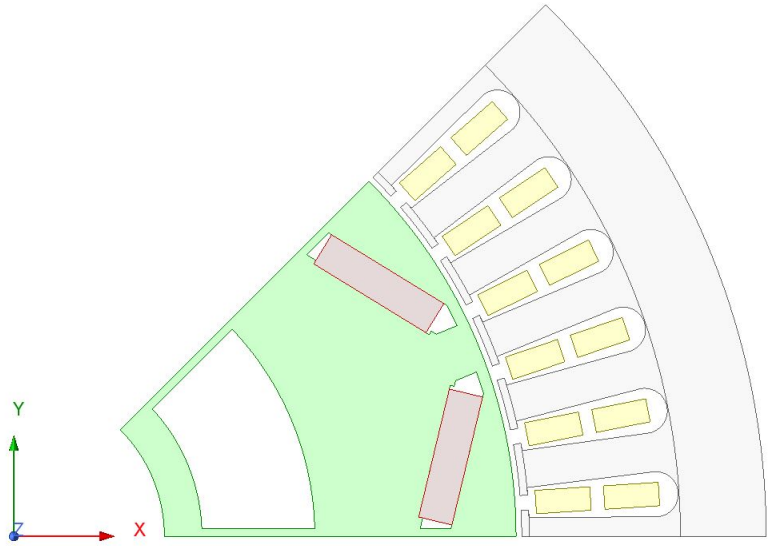

Figure 3.2: V shape IPMSM equipped with neodymium magnets

Table 3.2 provides the geometric and other design parameters needed for the construction of the V shape IPMSM.

Table 3.2: Geometric and other design parameters for V shape IPMSM

Parameter	Value
Stator outer dia(mm)	200
Stator inner dia(mm)	135
Rotor outer dia(mm)	133.5
Rotor inner dia(mm)	80
Stack length(mm)	127
Number of slots	48
number of poles	8
Number of turns	7
Number of parallel branches	4
Peak RMS current(A)	260
Max DC link voltage(V)	430
Magnet mass(Kg)	1.25

3.3 Scaling the motor

The geometric dimensions of the V-shaped IPMSM were used to rescale the FI-PMSM. The peak RMS current and maximum DC link voltage are 260 A and 430 V, respectively, values brought forward from the reference machine.The stack length of the machine is kept constant at 127 mm for all design iterations which is also brought forward from the reference machine. The stator, shown in Figure 3.3, remains the same for most of the design iterations. It will be modified in the future as per the design requirements and goals.

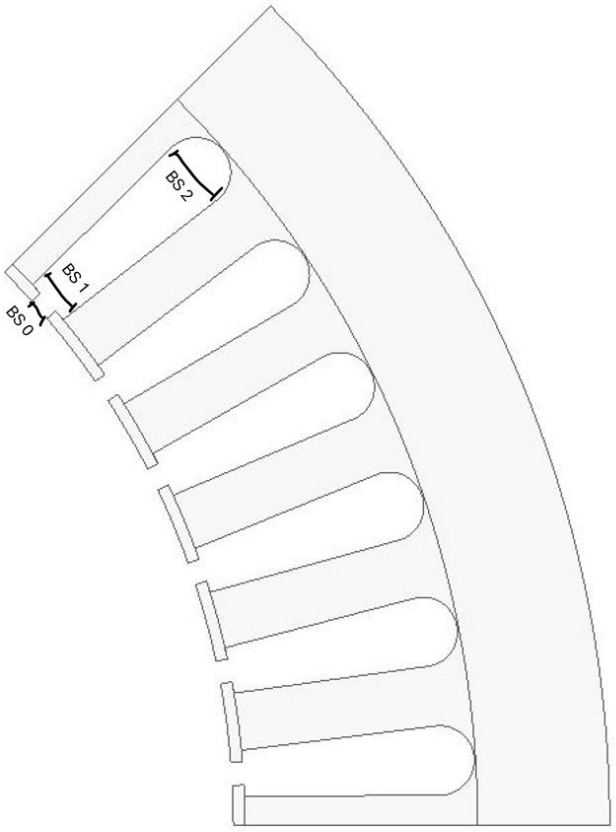

Figure 3.3: Reference stator design for different FI-PMSM design iterations

In figure 3.3, BS0 is the slot opening width, BS1 is the slot wedge maximum width and BS2 is the slot body bottom maximum width. From the literature, it was observed that using a 6-pole PMaSynRM with ferrite magnets in low-speed operation produced high torque and power output, so the 6-pole configuration was considered to be maintained for the FI-PMSM machine. The stator was modified from 48 slots to 36 slots for all FI-PMSM design iterations.

Table 3.3: Geometric dimensions of the stator

Parameter	Value
Stator outer dia(mm)	200
Stator inner dia(mm)	135
BS 2(mm)	6
BS 1(mm)	4
BS 0(mm)	2

The initial rotor design is based on the FI-PMSM from the literature but rescaled to match the geometric dimensions of the V-shaped IPMSM. The rotor design is modified in different design iterations to evaluate its effect on the motor's performance.

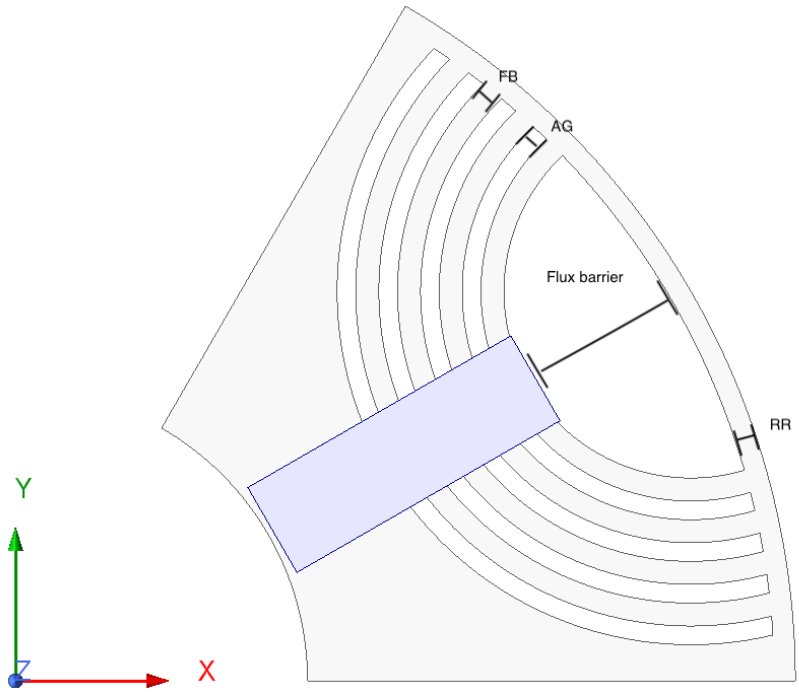

Figure 3.4: Reference rotor

In Figure 3.4, the term AG stands for Air Gap, FB for Flux Bridge, and RR for Rotor Ring. The geometric values of AG, FB, and RR vary across different rotor design iterations. The AG in the rotor is considered as one flux barrier ring. The number of flux barrier rings will vary for different rotor designs. The outer and inner diameter of the rotor are kept constant for majority of the designs.

3.4 Re scaled FI-PMSM equipped with neodymium magnets

The initial FI-PMSM from the literature was redesigned to match the geometric dimensions of the V-shaped IPMSM reference machine. The magnet mass in this machine was increased to maintain the same amount as in the V-shaped IPMSM, i.e., 1.25 kg. As the thickness of the magnets increased to match the magnet mass, it was observed that the torque ripple of the machine also increased. Figure 3.5 illustrates the redesigned FI-PMSM equipped with neodymium magnets.

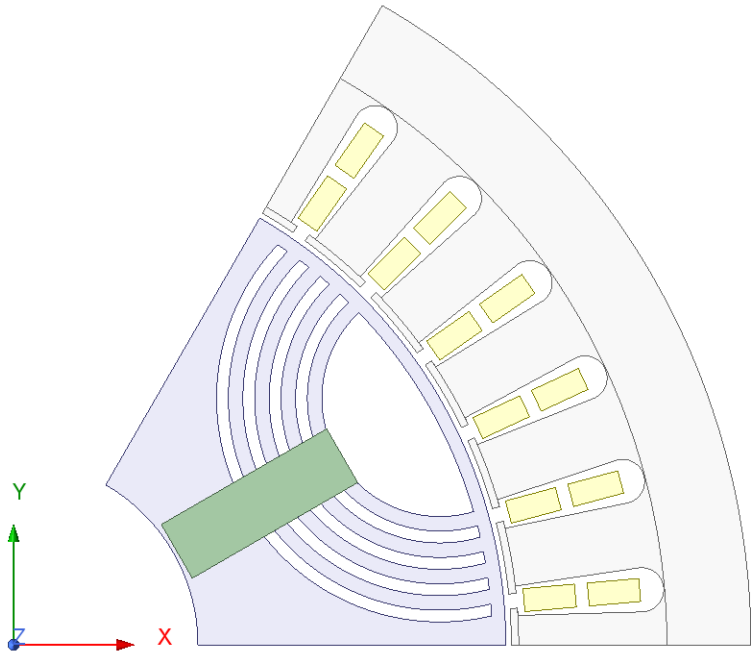

Figure 3.5: Re scaled FI-PMSM equipped with neodymium magnets

Table 3.4 provides information on the geometric dimensions and other key parameters for the construction of the machine.

Table 3.4: Geometric dimensions of re scaled FI-PMSM

Parameter	Value
Magnet mass(kg)	1.25
AG(mm)	1.6
FB(mm)	1.7
RR(mm)	1.8
Flux barrier(mm)	16
number of turns	6

The inner diameter of the rotor was reduced from 80 mm to 50 mm to accommodate

the magnet length. The magnet thickness could not be increased further due to the rising torque ripple. It was also observed that the design was suitable for neodymium magnets and well within saturation limits of the rotor and stator materials.

3.5 Investigated motor designs for FI-PMSM equipped with ferrite magnets

Different rotor designs that were investigated to improve the performance will be explained in this section. A Detailed explanation about their geometry changes will be mentioned.

3.5.1 Design 1 & 2

In the following rotor design, the geometry is the same as that of the re scaled FI-PMSM but equipped with ferrite magnets. The magnet dimensions remain the same, but the magnet mass is lower due to the lower density of the ferrite magnets. Figure 3.6 illustrates Rotor Design 1 for the FI-PMSM equipped with ferrite magnets.

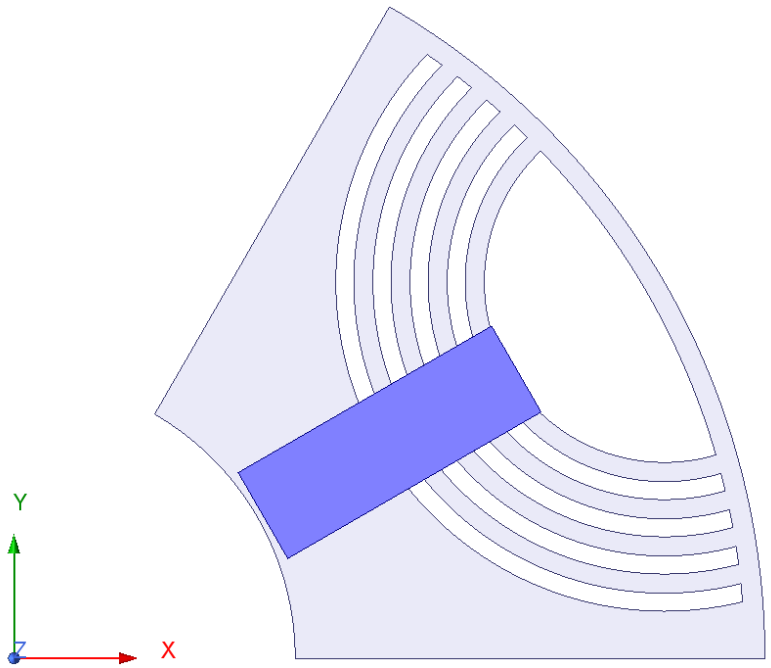

Figure 3.6: Design 1 of FI-PMSM equipped with ferrite magnets

Table 3.5 provides information on the geometric dimensions and other key parameters for the construction of the rotor design 1.

It is observed that there is saturation in some parts of the rotor ring and flux bridges. Therefore for design 2, the rotor ring thickness was increased slightly to

Table 3.5: Geometric dimensions of design 1

Parameter	Value
Magnet mass(kg)	0.83
AG(mm)	1.6
FB(mm)	1.7
RR(mm)	1.8
Flux barrier(mm)	16
number of turns	6

check the changes in saturation in the same regions and evaluate changes in its performance. Table 3.6 provides information on the geometric dimensions and other key parameters for the construction of the rotor design 2.

Table 3.6: Geometric dimensions of design 2

Parameter	Value
Magnet mass(kg)	0.83
AG(mm)	1.6
FB(mm)	1.7
RR(mm)	2
Flux barrier(mm)	16
number of turns	6

In Design 2, the saturation in the same region improved slightly, but the torque ripple increased. However, the overall torque decreased slightly. Table 3.7 presents the torque and torque ripple data for both Design 1 and Design 2.

Table 3.7: Torque and torque ripple figures for design 1 and design 2

Parameter	Design 1	Design 2	Difference(in %)
Torque(Nm)	102	100	-2
Torque ripple(Nm)	28	27	+2

3.5.2 Design 3,4 & 5

To further reduce saturation effects and improve flux linkage distribution in the rotor, an additional air gap ring was introduced. Rotor Designs 3, 4, and 5 have a 5-ring setup, with different air gap, flux barrier, and rotor ring thicknesses for each design. Figure 3.7 illustrates rotor Design 3, while rotor Designs 4 and 5 are similar in structure.

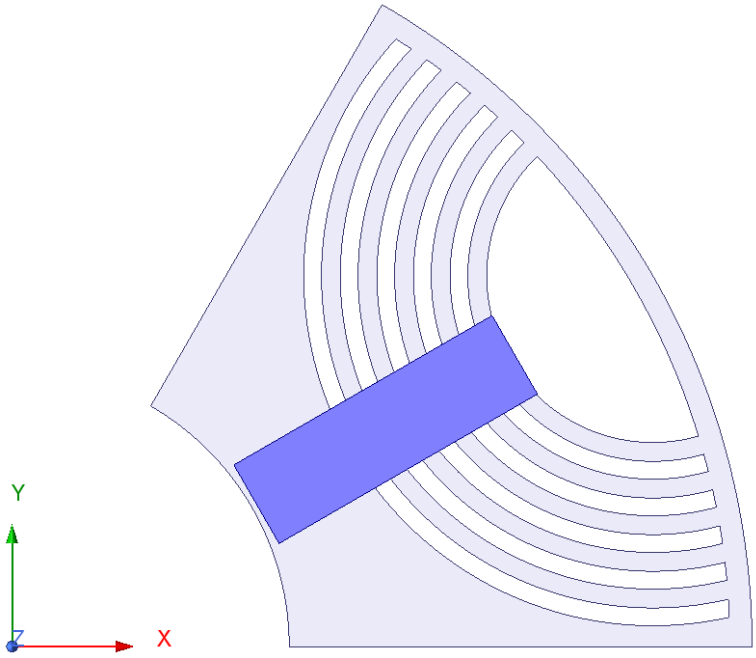

Figure 3.7: Design 3 of FI-PMSM equipped with ferrite magnets

In Designs 3, 4, and 5, the magnet thickness is decreased while the length is increased, in order to maintain the magnet mass. Table 3.8 provides information on the geometric dimensions and other key parameters for the construction of Rotor Designs 3, 4, and 5.

Table 3.8: Geometric dimensions of design 3,4 and 5

Parameter	Design 3	Design 4	Design 5
Magnet mass(kg)	0.8	0.81	0.8
AG(mm)	1.6	1.6	1.6
FB(mm)	1.7	1.7	1.9
RR(mm)	2	1.8	1.8
Flux barrier(mm)	15	15	15
Number of turns	6	6	6

Design 3 retained the same rotor ring thickness as Design 2 but included an additional ring. Design 4 also kept the original rotor ring thickness while following the same layout as Design 3. Design 5, however, featured an increased flux bridge thickness, with the rest of the design remaining the same as Design 4. Design 5 showed slightly reduced iron saturation compared to Designs 3 and 4. Improvements in both torque and torque ripple were observed across these designs. The 5-ring setup demonstrated reduced torque ripple compared to the 4-ring setup, linked to the placement of the air gap rings in relation to the stator teeth openings. Table 3.9 presents the torque and torque ripple data for Designs 3, 4, and 5.

Table 3.9: Torque and torque ripple figures for design 3,4 and 5

Parameter	Design 3	Design 4	Design 5
Torque(Nm)	104	106	104
Torque ripple(Nm)	14	14	12

It was observed that design 4 had a 2.5% increase in torque compared to design 5, but it should also be noted that there was a 1.2% increase in magnet mass. However, design 5 exhibited the lowest torque ripple, with a 12.6% improvement over design 4.

3.5.3 Design 6

The previous designs exhibited low iron saturation in the stator, which presented an opportunity to increase the stator teeth size. This could improve flux linkage and reduce copper losses. Hence, in Design 6, this possibility was investigated. At the same time, the rotor's outer diameter was slightly increased, and the stator's inner diameter was slightly reduced to explore the potential for improving torque. Figure 3.8 illustrates the geometrical design for rotor design 6.

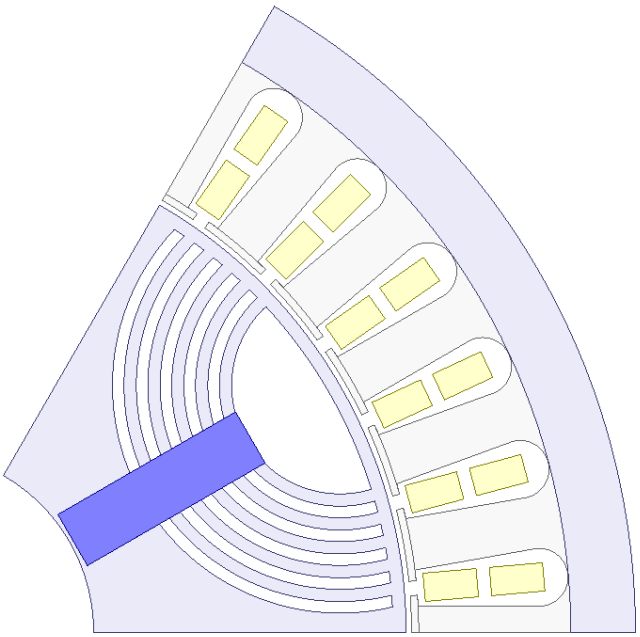

Figure 3.8: Design 6 of FI-PMSM equipped with ferrite magnets

Table 3.10 provides the geometric and other design parameters needed for the construction of the design 6.

Table 3.10: Geometric and other design parameters for design 6

Parameter	Value
Stator outer dia(mm)	200
Stator inner dia(mm)	138
Rotor outer dia(mm)	136.5
Rotor inner dia(mm)	80
Stack length(mm)	127
BS2(mm)	8
BS1(mm)	5
BS0(mm)	2
Number of turns	6
Magnet mass(kg)	0.8
AG(mm)	1.6
FB(mm)	1.7
RR(mm)	1.8
Flux barrier(mm)	15

The attempt to improve torque proved unsuccessful, but there was a 5% improvement in torque ripple compared to Design 5. However, there was a reduction in copper loss.

3.5.4 Design 7

It was observed that the area near the rotor shaft had a low flux density. To improve flux density in this region, ring 5 (the outermost ring) was extended toward the shaft. The rest of the design remained similar to that of design 5. Figure 3.9 illustrates the geometric layout of rotor design 7.

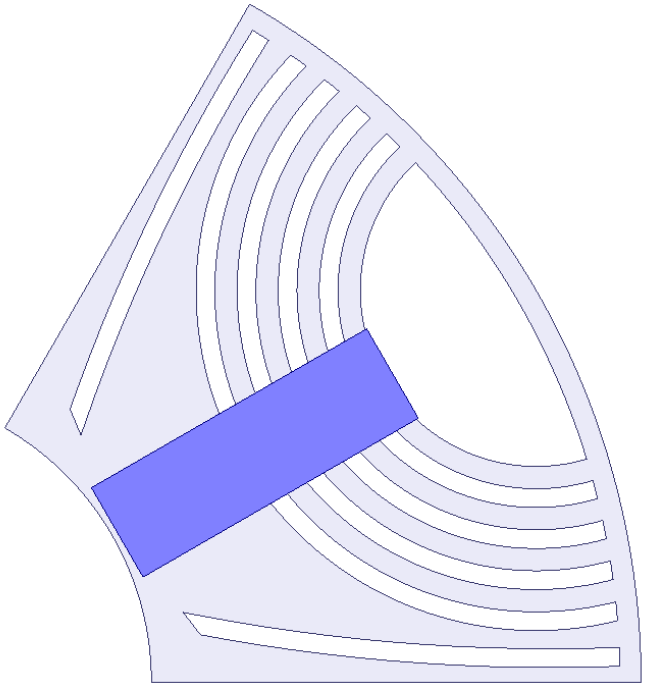

Figure 3.9: Design 7 of FI-PMSM equipped with ferrite magnets

Table 3.11 provides the geometric and other design parameters needed for the construction of the rotor design 7.

Table 3.11: Geometric and other design parameters for design 7

Parameter	Value
Magnet mass(kg)	0.85
AG(mm)	1.6
FB(mm)	1.9
RR(mm)	1.8
Flux barrier(mm)	15

Table 3.12 compares the torque and torque ripple of design 5 and 7. Design 7 did

Table 3.12: Torque and torque ripple comparison of design 5 and design 7

Parameter	Design 5	Design 7
Torque(Nm)	104	101
Torque ripple(Nm)	12	8

not show significant improvement in overall magnetic flux linkage. However, there was a 34% reduction in torque ripple and a 1% decrease in overall torque.

3.6 Demagnetisation setup

As discussed earlier in Section 2.6, demagnetization occurs due to an external field in the wrong direction. Ferrite magnets are at higher risk of demagnetization at lower temperatures. The critical flux at 20°C ranges from 0.013 T to 0.016 T. It has been observed that increasing the q-axis current results in a very low risk of demagnetization, whereas increasing negative d-axis current poses a higher risk. Therefore, to assess the risk of demagnetization beyond safe operating regions, the q-axis current is kept constant at 0, and the negative d-axis current is increased up to the peak RMS current to evaluate the risk of demagnetization at each point.

4

Analysis

This chapter will give a detailed explanation of all the simulated results and their comparisons.

4.1 V shape IPMSM

This section presents the results of the V-shaped machine equipped with both neodymium and ferrite magnets, along with a comparison between them.

To analyze the machine in Ansys Electronics and retrieve the necessary data, a parametric sweep of i_d and i_q is performed. The number of turns and conductors in series are specified. The data imported from Ansys Electronics consists of transient 3-phase quantities, which are a function of different combinations of i_d and i_q. Table 4.1 lists the quantities imported from Ansys.

Table 4.1: Quantities imported from Ansys Electronics

Parameter	Unit
Time	Sec
3-phase flux linkages	Wb
3-phase induced voltages	V
3-phase input current	A
Torque	Nm
Core loss	W
Eddy current loss	W
Hysteresis loss	W
Solid loss	W
Copper loss	W
Mechanical position	rad

A simulation was carried out to check the magnetic flux by setting the d-axis current to 0 and varying the q-axis current from 0 to 400 in steps of 50, while maintaining a constant current angle. In the absence of an external field, the magnetic flux in the

d-axis direction is solely due to the magnets. Figure 4.1 illustrates the comparisson of the magnetic flux of two different magnetic materials.

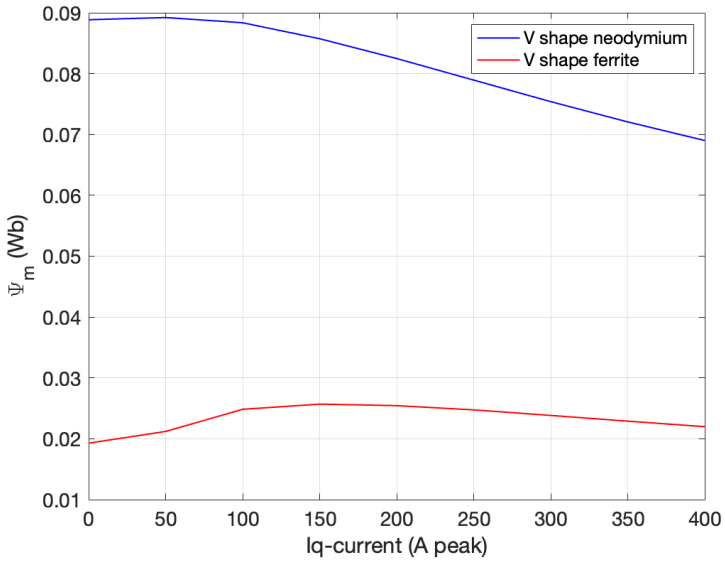

Figure 4.1: Magnetic flux linkages of V shape IPMSM equipped with two different magnets

Magnetic flux is a key parameter in deriving magnetic torque. It has been observed that the magnetic flux from neodymium magnets is nearly four times greater than that of ferrite magnets, indicating the ability to obtain a higher output torque. Field-oriented control (MTPA) was used to define the operating region of the machines and to reduce resistive losses. Figures 4.2 and 4.3 show the operating regions of the machines equipped with neodymium and ferrite magnets, respectively.

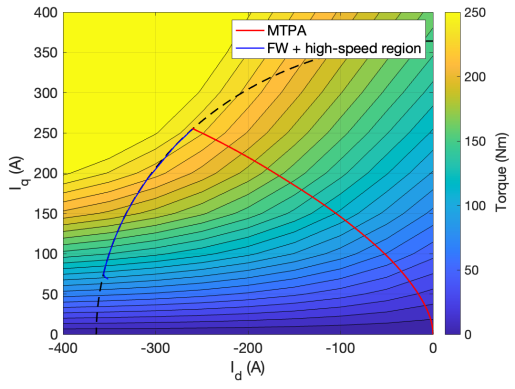

Figure 4.2: Operating region for V shape IPMSM equipped with neodymium magnets

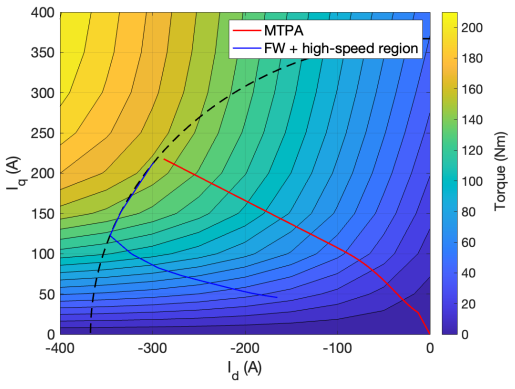

Figure 4.3: Operating region for V shape IPMSM equipped with ferrite magnets

The operating regions are plotted on the d-q plane, with contours representing

the torque output and the circular boundary indicating the current limit. Torque values for various i_d and i_q combinations were obtained from simulations and later interpolated to map the entire torque vs. speed regions with high resolution. A speed step of $n_{\text{step}} = 500$ RPM and a torque step of $T_{\text{step}} = 10$ Nm were used. Figure 4.4 shows the torque vs. speed and power vs. speed plots for the V-shaped machine equipped with two different magnets.

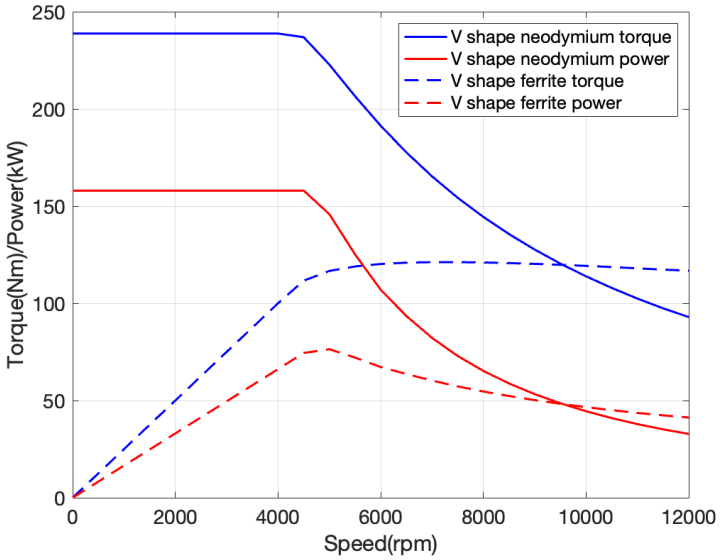

Figure 4.4: Torque vs power vs speed curve for a V shape machine equipped with two different magnet materials.

The plot shows that the torque output of the ferrite magnet is 33% lower than that of the V-shaped machine equipped with neodymium magnets, while the power output is 37% lower. Both machines begin field weakening at 4500 RPM. The total loss for each machine is the sum of copper losses, eddy current losses, and hysteresis losses. Copper loss is calculated analytically as the product of stator resistance and the square of the RMS currents at different speeds, noting that copper losses are frequency-dependent. To account for core lamination degradation, iron losses are multiplied by a factor of 1.7, making the result more realistic. The losses are obtained from simulations at one speed point and then scaled using a factor to interpolate and estimate losses across different speeds, mapping the losses for the entire torque-speed range. The scaling factor is the ratio of the current simulation speed to the speed at which the loss is being calculated. Figure 4.5 and 4.6 illustrate the total losses over the entire operating region for V shape equipped with neodymium and ferrite magnets respectively.

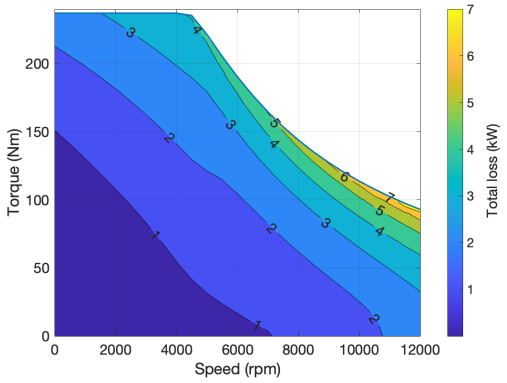

Figure 4.5: Loss map for V shape IPMSM equipped with neodymium magnets

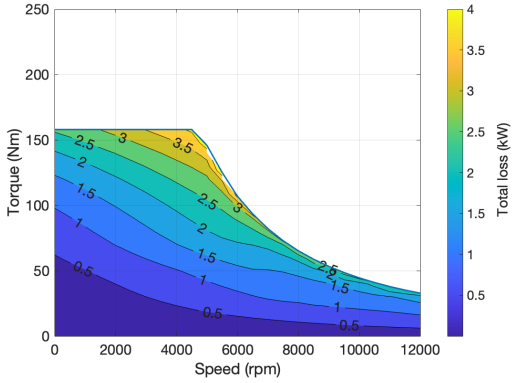

Figure 4.6: Loss map for V shape IPMSM equipped with ferrite magnets

It can be observed from the plots that the machine equipped with ferrite magnets has higher losses in the high-torque, low-speed region and lower losses in the low-torque, high-speed region compared to the machine with neodymium magnets. The efficiency of these machines is calculated as the ratio of mechanical output power to input electrical power. Figures 4.7 and 4.8 illustrate the efficiency across the entire operating regions for the V-shaped machine equipped with neodymium and ferrite magnets, respectively.

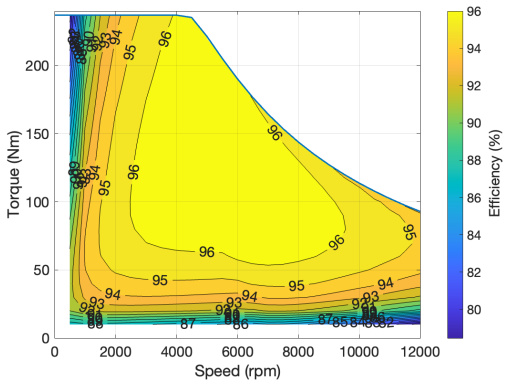

Figure 4.7: Efficiency map for V shape IPMSM equipped with neodymium magnets

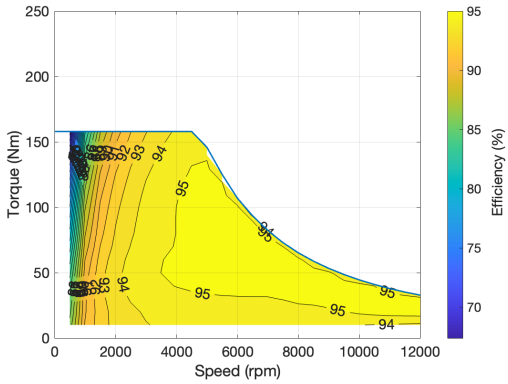

Figure 4.8: Efficiency map for V shape IPMSM equipped with ferrite magnets

4.2 Rescaled FI-PMSM equipped with neodymium magnets

The simulation was conducted by performing a parametric sweep of i_d and i_q from -400 to 400, with a current step of 50. The magnetic flux in the q direction was

calculated at time steps of 50 as well. Figure 4.9 illustrates the magnetic flux linkage of the re-scaled FI-PMSM.

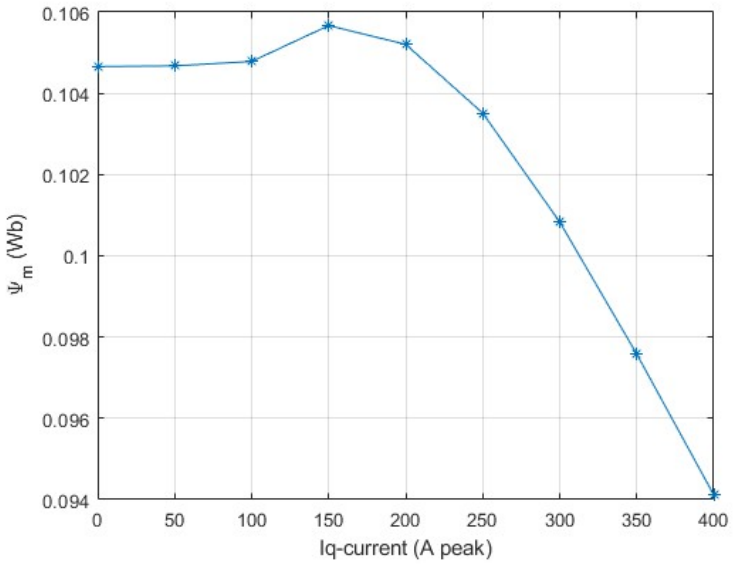

Figure 4.9: Magnetic flux linkage in q-axis direction for a FI-PMSM equipped with neodymium magnets

It can be seen that the magnetic flux is high at even i_q is equal to 0 indicating possibility of having high efficiency in low speed low torque region. The MTPA control strategy is used to plot the entire operating region of the machine. Figure 4.10 illustrates the entire operating region for the machine.

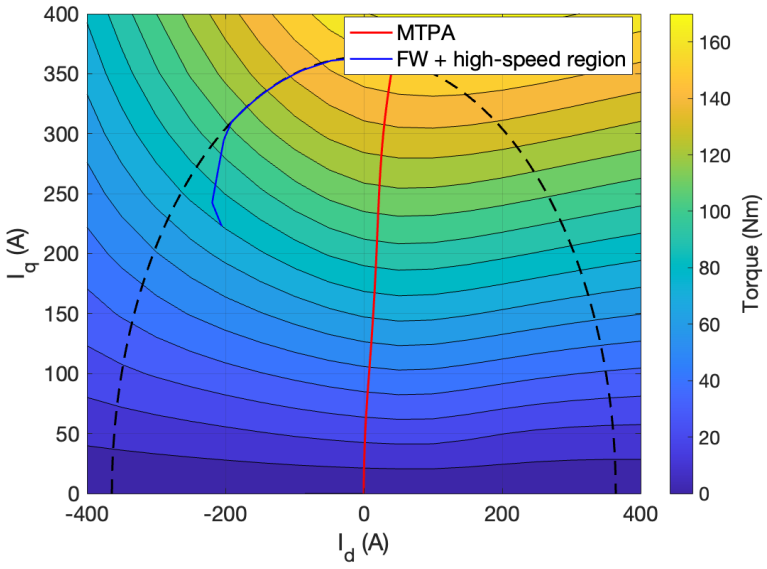

Figure 4.10: Operating region for a FI-PMSM equipped with neodymium magnets

It can be seen that the magnetic flux remains high even under load, as the constant torque region lies in the first quadrant where positive d-axis current is applied. Using the operating region, the torque is interpolated at corresponding i_d and i_q values at different speeds to plot the torque vs. speed and power vs. speed curves. The field weakening point is also visible in this plot. Figure 4.11 illustrates the torque vs. speed and power vs. speed mapping.

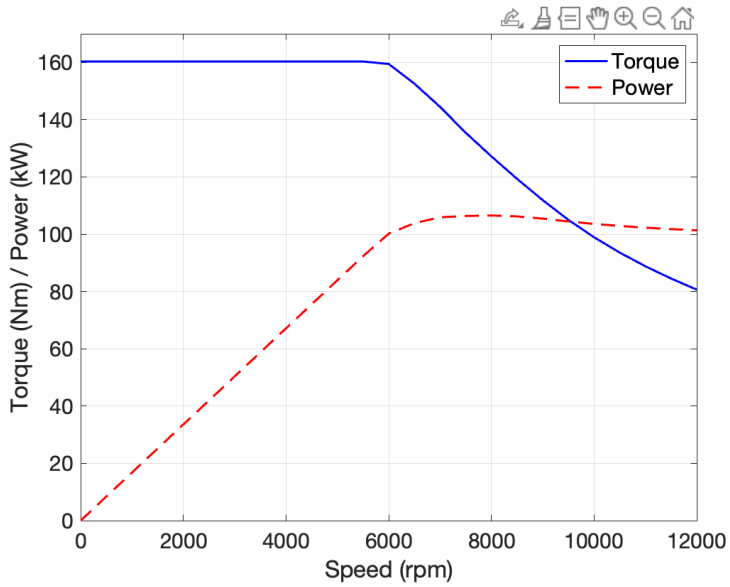

Figure 4.11: Torque vs power vs speed curve for a FI-PMSM equipped with neodymium magnets

The mapping was carried out with a torque step of 10 Nm and speed steps of 500 RPM. The machine's rated torque is observed to be 161 Nm, with a rated power of 105 kW. Field weakening begins at 6000 RPM. The losses and efficiency are calculated in the same manner as for the V-shaped machine. Figures 4.12 and 4.30 illustrate the total loss and efficiency plots for the machine's entire operating region, respectively.

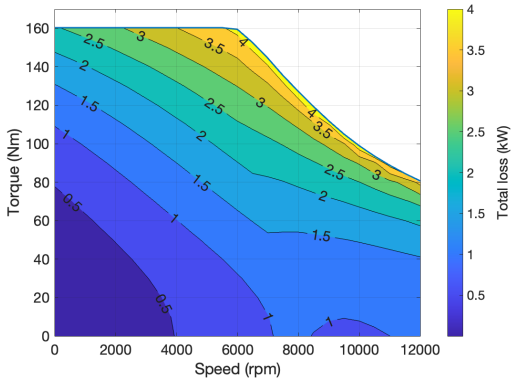

Figure 4.12: Loss map for FI-PMSM equipped with neodymium magnets

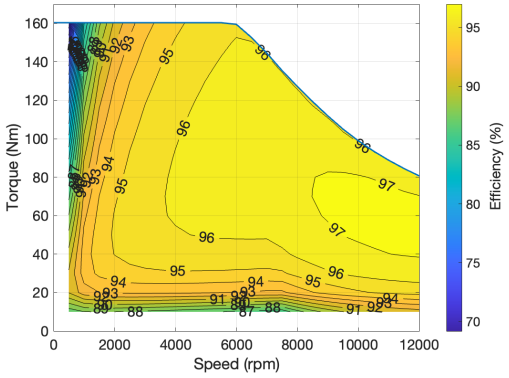

Figure 4.13: Efficiency map for FI-PMSM equipped with neodymium magnets

The efficiency in the high-speed, low-torque region is significantly higher. And the overall efficiency is observed to be high as well.

4.3 FI-PMSM equipped with ferrite magnets

This section presents the results of various design iterations equipped with ferrite magnets.

Three notable designs are selected for performance comparison: Design 1, Design 5, and Design 7, which are renamed as Design A, Design B, and Design C, respectively, to simplify the comparison. Table 4.2 provides a comparison of the different design iterations for the FI-PMSM equipped with ferrite magnets.

Table 4.2: Comparison of design A,B and C

Parameter	Design A	Design B	Design C
Magnet mass(kg)	0.8	0.81	0.8
AG(mm)	1.6	1.6	1.6
FB(mm)	1.7	1.7	1.9
RR(mm)	2	1.8	1.8
Torque	104	102	101
Torque ripple	28	12	8

It is observed that all designs have a similar torque output. However, it is worth noting that the torque ripple in Design B is reduced by 56% compared to Design A. Figures 4.14 and 4.15 illustrate the magnetic flux linkages and the torque-speed and power-speed curves for the different designs, respectively.

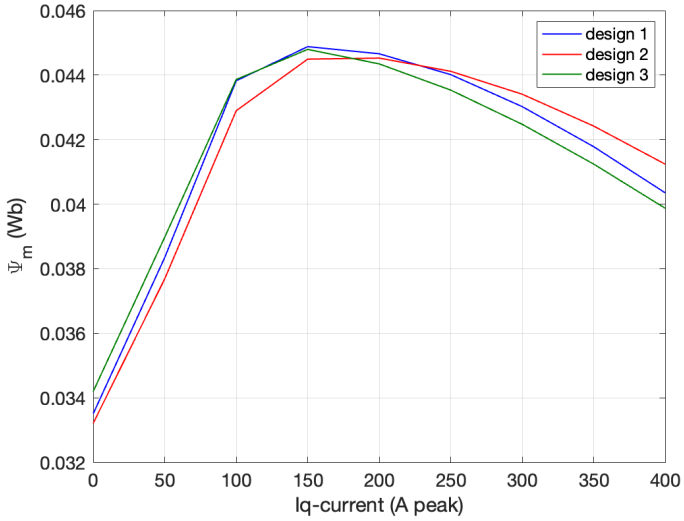

Figure 4.14: Magnetic flux linkages for different rotor designs of FI-PMSM equipped with ferrite magnets

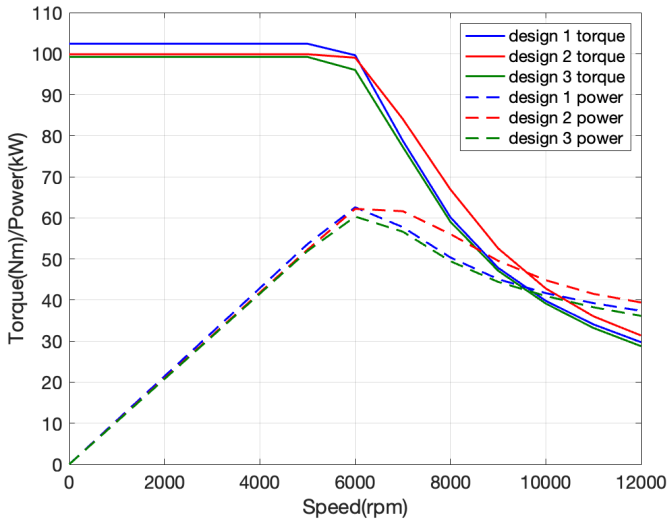

Figure 4.15: Torque speed and power speed curves for different rotor designs of FI-PMSM equipped with ferrite magnets

It is observed that the magnetic flux linkage for design A reaches its peak value at a lower q-axis current. Additionally, the peak torque achieved by design A is 104 Nm, which is 2% higher than that of design B and design C. However, design B has the highest power output of 63 kW, which is 1% higher than both design A and design C. Figures 4.16, 4.24, and 4.18 illustrate the efficiencies across the operating regions for design A, design B, and design C, respectively.

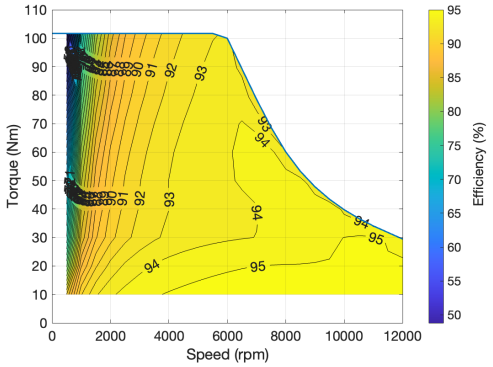

Figure 4.16: Efficiency map for design A

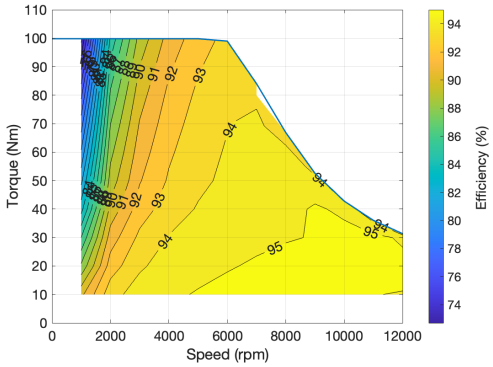

Figure 4.17: Efficiency map for design B

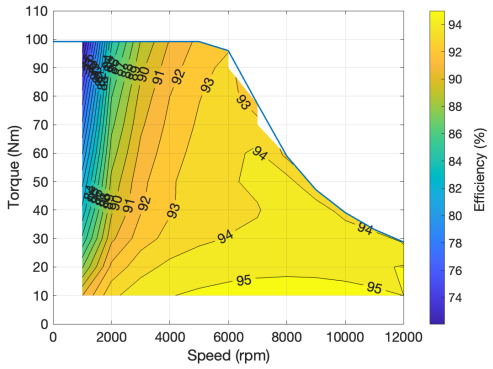

Figure 4.18: Efficiency map for design C

From the efficiency plots, it can be seen that all designs achieve high efficiency in the high-speed, low-torque region. However, design B shows higher efficiency in this area compared to the other two designs. Considering the overall performance of design B, it has been selected for further analysis.

4.3.1 Parametric sweep of design B

Design B was selected for a parametric analysis of magnet thickness and magnet mass. Three different magnet masses were tested: one from the previous analysis, one with a lower mass, and another with the same magnet mass as the V-shaped ferrite design. Table 4.3 outlines the different magnet masses used for the parametric sweep.

Table 4.3: Different magnet mass quantities for design B

Design names	Magnet mass
Design B_1	0.8kg
Design B_2	0.7kg
Design B_3	1.25kg

Figures 4.19 and 4.20 illustrate the magnetic flux linkage, as well as the torque-speed and power-speed curves, for the different magnet thickness parametric sweeps of design B.

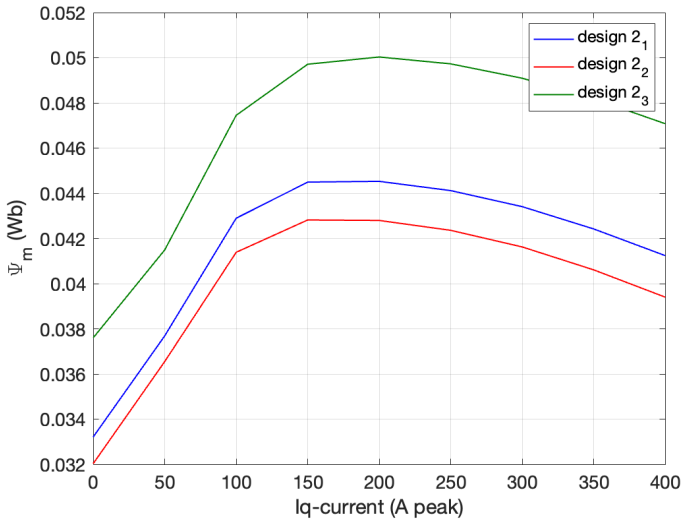

Figure 4.19: Magnetic flux linkages for different magnet thickness

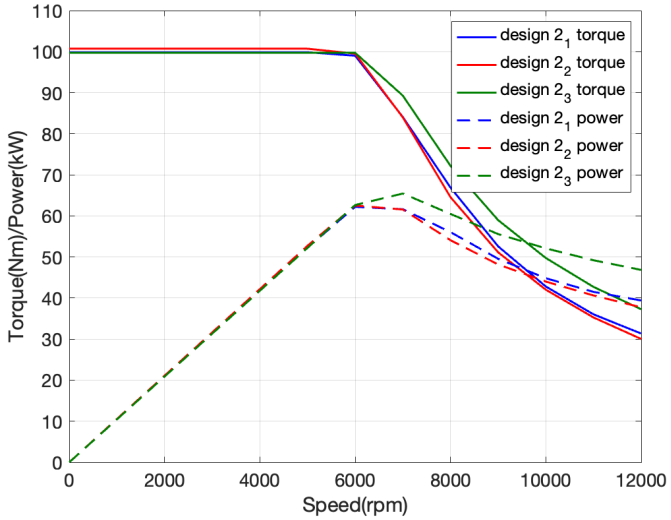

Figure 4.20: Torque speed and power speed curves for different magnet thickness

Figure 4.19 shows that the flux linkage is highest for design B_3, but the torque output for all magnet masses remains similar. However, design B_2, which has the lowest magnet mass and thickness, exhibits 2% higher torque compared to Design B_3, despite having 44% less magnet mass. This can be explained by the contribution of reluctance torque, driven by the difference in inductance between the d-axis and q-axis directions. Figures 4.21, 4.22, and 4.23 illustrate the inductance difference

along the d-axis and q-axis for design B_1, design B_2, and design B_3, respectively.

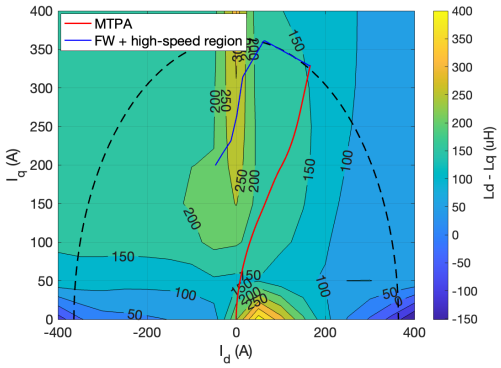

Figure 4.21: (L_d-L_q) for design B_1

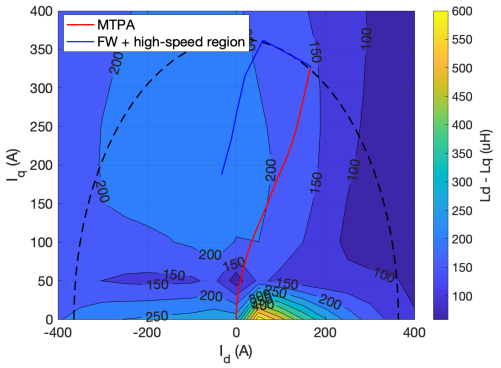

Figure 4.22: (L_d-L_q) for design B_2

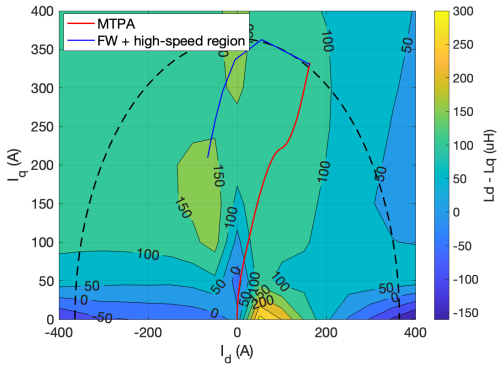

Figure 4.23: (L_d-L_q) for design B_3

From these plots, it can be observed that the difference in inductance between the d-axis and q-axis in the constant torque region for design B_2 is greater than that of design B_3. This results in a higher reluctance torque contribution, leading to an overall increase in torque. Figures 4.16, 4.25 and 4.26 illustrate the efficiency maps for design B_1, design B_2 and design B_3 respectively.

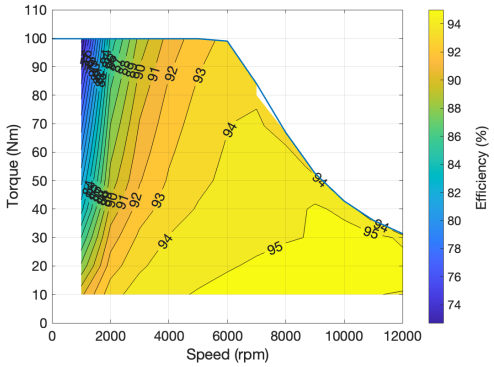

Figure 4.24: Efficiency map for design B_1

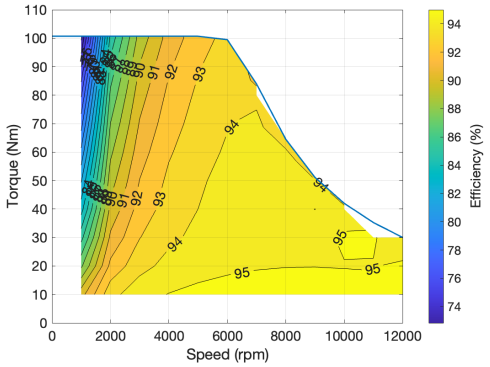

Figure 4.25: Efficiency map for design B_2

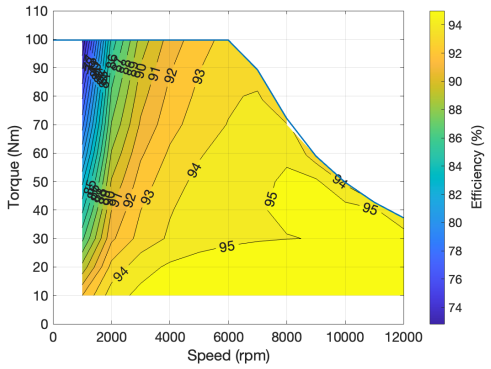

Figure 4.26: Efficiency map for design B_3

The plots show that all three designs exhibit higher efficiency in the high-speed, low-torque region, with design B_3 having the highest efficiency among them. Considering all performance factors, design B_3, with a magnet mass of 1.25 kg, was selected for further comparison against the FI-PMSM equipped with neodymium magnets and the V-shaped IPMSM equipped with ferrite magnets.

4.4 Comparison of V shape ferrite vs FI-PMSM noedymium vs FI-PMSM ferrite

This section will compare the different machines with their respective final selected designs. Table 4.4 describes the key design parameters for the different motor designs.

Table 4.4: Comparison of V shape ferrite, FI-PMSM neodymium and FI-PMSM ferrite

Parameter	V shape ferrite	FI-PMSM neodymium	FI-PMSM ferrite
Magnet material	FB9B	NMX 37F	FB9B
Magnet mass(kg)	1.25	1.25	1.25
stack length	127	127	127
number of turns	7	6	7.5
Peak RMS current	260	260	260
DC link voltage	430	430	430

It can be observed that the number of turns is not equal, which may impact the overall torque output of each machine. The number of turns in the final design was adjusted to harmonize the field weakening points, enabling a more accurate comparison of each machine. Figures 4.27 and 4.28 illustrates the magnetic flux linkage and torque speed and power speed curves for the different machines.

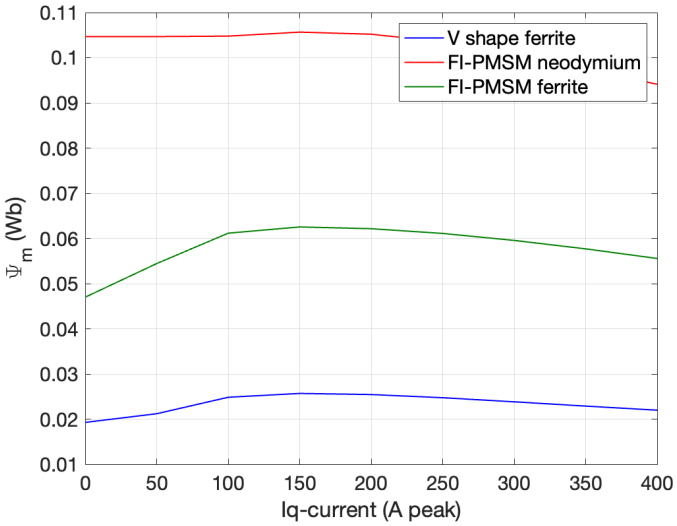

Figure 4.27: Magnetic flux linkages for V shape ferrite, FI-PMSM neodymium and FI-PMSM ferrite

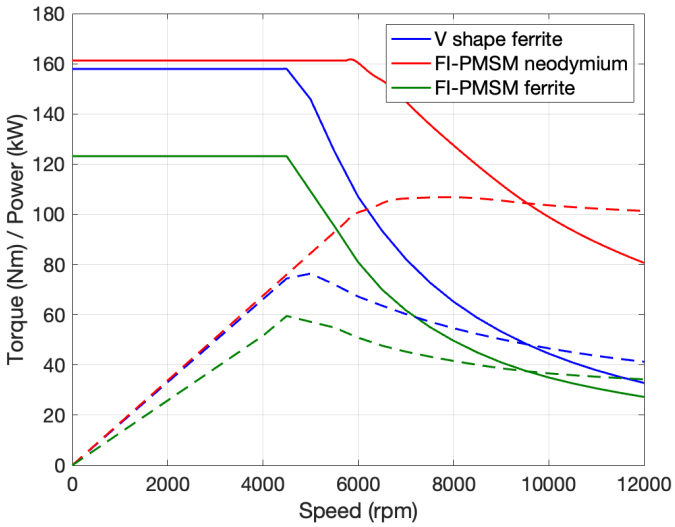

Figure 4.28: Torque speed and power speed curves for V shape ferrite, FI-PMSM neodymium and FI-PMSM ferrite

The plots show that the magnetic flux linkage for the FI-PMSM with neodymium magnets is nearly five times that of the V-shaped ferrite machine, yet the torque output of the FI-PMSM neodymium is only 1.25% higher than the V-shaped ferrite machine. The peak torque for the V-shaped ferrite machine is 158 Nm, for the FI-PMSM with neodymium magnets it is 160 Nm, and for the FI-PMSM with ferrite magnets it is 130 Nm. The power output is 79 kW for the V-shaped ferrite, 110 kW for the FI-PMSM neodymium, and 60 kW for the FI-PMSM ferrite. Figures 4.29, 4.30 and 4.31 illustrate the efficiency maps for the V shape ferrite, FI-PMSM neodymium and FI-PMSM ferrite machines respectively.

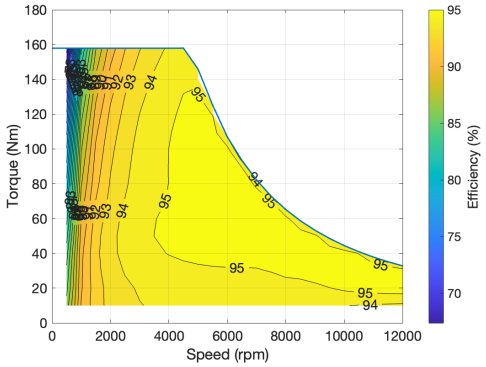

Figure 4.29: Efficiency map for V shape ferrite

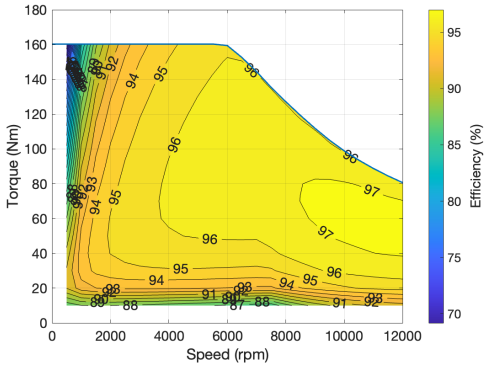

Figure 4.30: Efficiency map for FI-PMSM neodymium

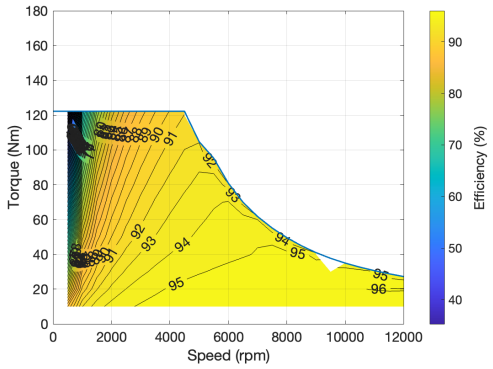

Figure 4.31: Efficiency map for FI-PMSM ferrite

It is observed that the V-shaped ferrite machine has higher efficiency in the low-speed, high-torque region compared to the FI-PMSM with ferrite magnets. However, the latter shows higher efficiency in the high-speed, low-torque region. Overall, the FI-PMSM with neodymium magnets exhibits the highest efficiency across most operating regions.

4.5 Demagnetisation study

The risk of irreversible demagnetization of ferrite magnets was assessed in the operating regions by testing the V-shaped ferrite machine and the FI-PMSM ferrite with two different magnet thicknesses. Two operating points were selected for evaluation: one at i_d = -260 (the peak RMS current) and the other at i_d = -250. Figures 4.32, 4.33, and 4.34 illustrate the flux densities and their flux directions for design B_1, design B_3, and the V-shaped ferrite machine at i_d = -260.

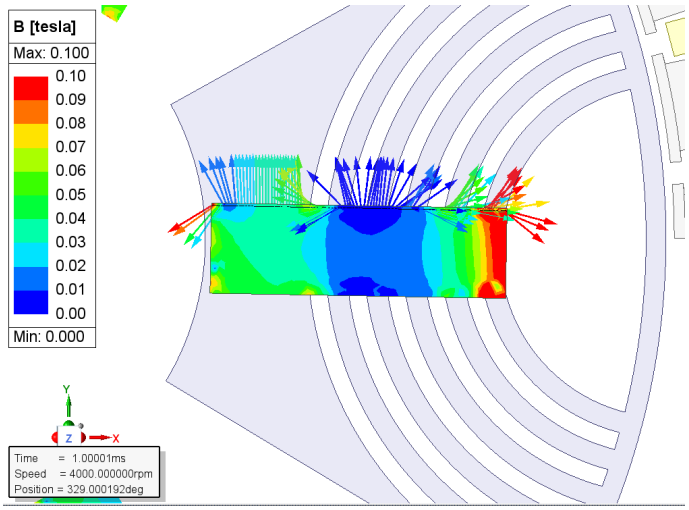

Figure 4.32: Demagnetisation study of design B_1 at i_d=-260

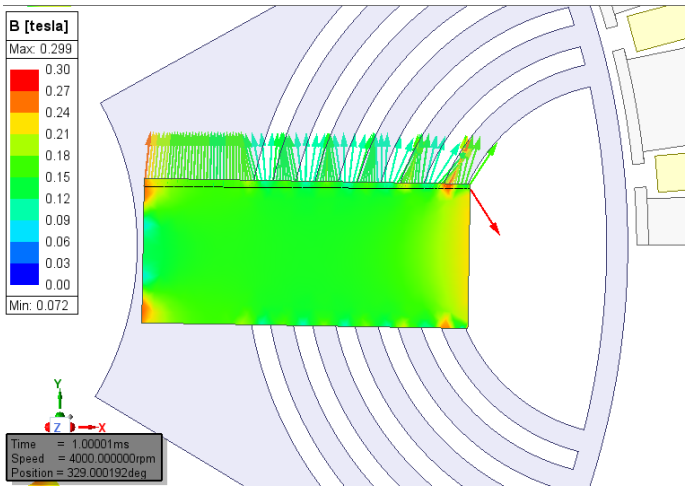

Figure 4.33: Demagnetisation study of design B_3 at i_d=-260

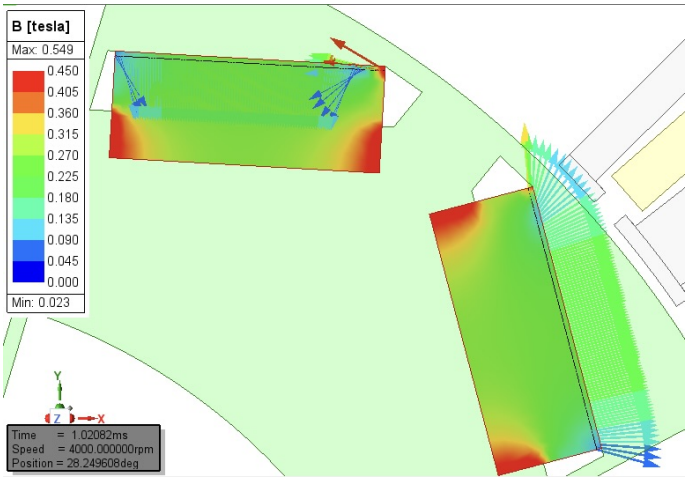

Figure 4.34: Demagnetisation study of V shape ferrite at i_d=-260

It is observed that when i_d = -260 for design B_1 (with the lower magnet thickness), demagnetization occurs in certain areas as the magnet flux density drops below 0.01 T. In contrast, design B_3 (with the higher magnet thickness) does not experience demagnetization, as seen the flux density remains above 0.08 T in all regions of the magnet. This highlights the critical role that magnet thickness plays in preventing demagnetization. Additionally, the V-shaped ferrite machine demonstrates better performance than design B_1 in handling negative d-axis current and avoiding demagnetization. Figures 4.35, 4.36, and 4.37 illustrate the flux densities and their flux directions for design B_1, design B_3, and the V-shaped ferrite machine at i_d = -250.

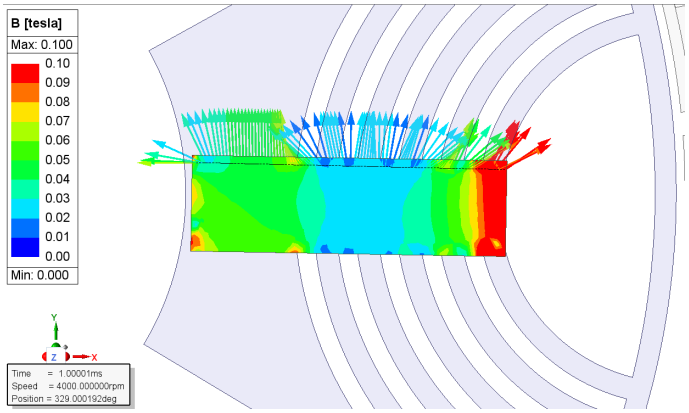

Figure 4.35: Demagnetisation study of design B_1 at i_d=-200

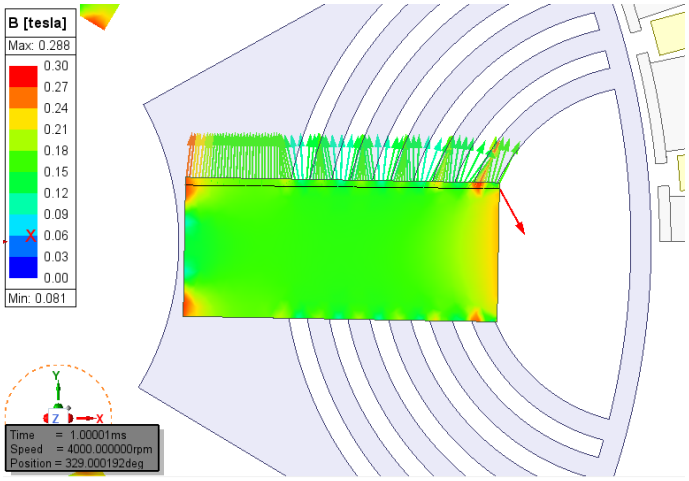

Figure 4.36: Demagnetisation study of design B_3 at i_d=-200

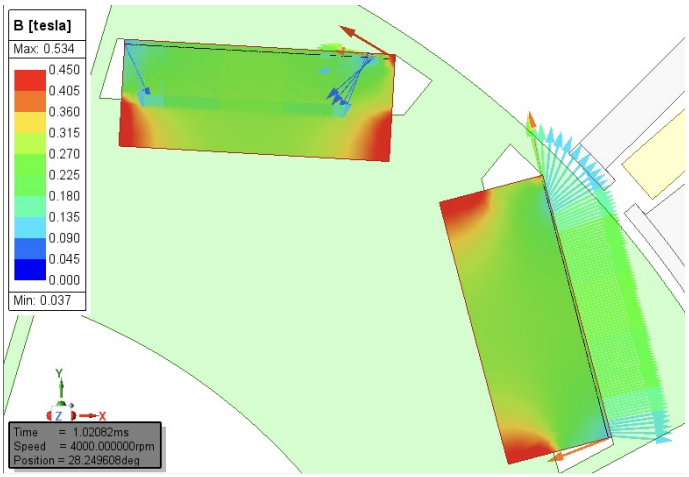

Figure 4.37: Demagnetisation study of V shape ferrite at i_d=-200

The designs were studied at i_d = -250, where it was observed that design B_1 just begins to demagnetize, with flux density in some areas dropping below 0.01 T. At this same current, design B_3 and the V-shaped ferrite machine were also tested to assess their behavior. Design B_3 showed no signs of demagnetization, maintaining higher flux densities, while the V-shaped ferrite machine demonstrated better resilience against demagnetization than design B_1.

5

Conclusion

5.1 Results

In this thesis, an FI-PMSM was constructed using ferrite magnets to evaluate its performance and resistance to demagnetization when negative d-axis current is applied within its operating region. Several rotor designs were explored, and the most promising design was compared against an FI-PMSM equipped with neodymium magnets and a V-shaped IPMSM using ferrite magnets. These machines were evaluated based on their rated torque, efficiency, and ability to withstand demagnetization.

The study found that the FI-PMSM equipped with ferrite magnets had a 24% lower rated torque and a 45% lower rated power compared to the FI-PMSM with neodymium magnets. Additionally, it demonstrated a 23% lower rated torque and a 23% lower rated power than the V-shaped IPMSM with ferrite magnets. In terms of efficiency, the FI-PMSM with ferrite magnets exhibited lower efficiency than the neodymium-equipped FI-PMSM in the high-speed, low-torque region, but outperformed the V-shaped ferrite IPMSM in this same region.

Regarding risk of irreversible demagnetization, the FI-PMSM with ferrite magnets showed better resilience with thicker magnets, but overall, it presented a higher risk of demagnetization compared to the V-shaped IPMSM with ferrite magnets.

5.2 Future work

The results from this thesis are based on the specific requirements and assumptions made throughout the study. Further optimization of the rotor designs for the FI-PMSM equipped with ferrite magnets could help reduce torque ripple and mitigate the risk of irreversible demagnetization. One area for improvement involves optimizing the spacing of the air gap rings to reduce torque ripple. Additionally, increasing the number of air gap rings by reducing their thickness could potentially enhance performance while lowering the risk of demagnetization.

With the availability of more advanced ferrite magnets on the market, these could be

tested to assess their potential for improved performance. Considering the favorable magnetic flux linkage characteristics observed in the FI-PMSM with ferrite magnets, the designs could be tested in drive cycles to evaluate their efficiency in the low-speed, low-torque regions, where performance is expected to be better.

Finally, different orientations of magnet placement should be explored to examine their effects on demagnetization risk. This could provide further insights into ways to optimize machine design and performance while minimizing demagnetization vulnerability.

Bibliography

[1] Torbjörn Thiringer,Emma Grunditz & Joachim Lindström (2017), Field intensified PM machine for a HEV application.

[2] Praveena Pandurangan & Nikhil Manakshya (2021),Permanent magnet synchronous machine using ferrite vs rare earth magnets-how do they compare?

[3] Elias Kambrin & Anton Ingemansson (2022),Comparison of a highly sustainable PMaSynRM with a traditional PMSM

[4] https://hir.harvard.edu/not-so-green-technology-the-complicated-legacy-of-rare-earth-mining/

[5] https://www.greatmagtech.com/info/the-environmental-impact-of-neodymium-magnets-81078752.

[6] https://www.emobility-engineering.com/reduced-rare-earth-and-magnet-free-motors/

[7] N. Limsuwan, T. Kato, K. Akatsu and R. D. Lorenz, "Design and evaluation of a variable-flux flux-intensifying interior permanent magnet machine," 2012 IEEE Energy Conversion Congress and Exposition (ECCE), Raleigh, NC, USA, 2012, pp. 3670-3677, doi: 10.1109/ECCE.2012.6342480.

[8] T. Kato, N. Limsuwan, C. -Y. Yu, K. Akatsu and R. D. Lorenz, "Rare Earth Reduction Using a Novel Variable Magnetomotive Force Flux-Intensified IPM Machine," in IEEE Transactions on Industry Applications, vol. 50, no. 3, pp. 1748-1756, May-June 2014, doi: 10.1109/TIA.2013.2283314.

[9] K. Akatsu, M. Arimitsu, and S. Wakui, “Design and control of a field-intensified interior permanent-magnet synchronous machine,” IEEJ Trans. Ind. Appl., vol. 126, no. 7, pp. 827–834, Jul. 2006.

[10] H. Liu, H. Lin, S. Fang, and Z. Q. Zhu, “Permanent-magnet demagnetization physics of a variable-flux memory motor,” IEEE Trans. Magn., vol. 45, no. 10, pp. 4736–4739, Oct. 2009.

[11] Fukushige, T.,Limasuwan, N., Kato, T., Akatsu, K., Lorentz, R.D., “ Efficiency Contours and Loss Minimization Over a Drive Cycle of a Variable Flux-Intensifying Machine”, IEEE Transaction on Industry Applications, Vol. 51, No.4, July7August 2015 2014, p.2948-2989

[12] https://www.eclipsemagnetics.com/resources/guides/rare-earth-magnets-vs-regular-magnets/

[13] https://www.stanfordmagnets.com/ferrite-magnets-exploring-their-pros-and-cons-across-industries.html

[14] E. A. Grunditz, S. T. Lundmark, M. Alatalo, T. Thiringer and A. Nordelöf, "Three traction motors with different magnet materials — Influence on cost, losses, vehicle performance, energy use and environmental impact," 2018 Thirteenth International Conference on Ecological Vehicles and Renewable Energies (EVER), Monte Carlo, Monaco, 2018, pp. 1-13, doi: 10.1109/EVER.2018.8362387.

[15] T. Tokuda, M. Sanada and S. Morimoto, "Influence of rotor structure on performance of permanent magnet assisted synchronous reluctance motor," 2009 International Conference on Electrical Machines and Systems, Tokyo, Japan, 2009, pp. 1-6, doi: 10.1109/ICEMS.2009.5382889.

DEPARTMENT OF ELECTRICAL ENGINEERING
CHALMERS UNIVERSITY OF TECHNOLOGY
Gothenburg, Sweden
www.chalmers.se

CHALMERS
UNIVERSITY OF TECHNOLOGY